

Research Article

A Modified Unscented Kalman Filter Combined with Ant Lion Optimization for Vehicle State Estimation

Yixi Zhang , Jian Ma , Xuan Zhao , Xiaodong Liu , and Kai Zhang 

School of Automobile, Chang'an University, Xi'an 710064, Shaanxi, China

Correspondence should be addressed to Jian Ma; majian@chd.edu.cn and Xuan Zhao; zhaoxuan@chd.edu.cn

Received 8 September 2020; Revised 23 September 2020; Accepted 10 December 2020; Published 5 January 2021

Academic Editor: Xingling Shao

Copyright © 2021 Yixi Zhang et al. This is an open access article distributed under the Creative Commons Attribution License, which permits unrestricted use, distribution, and reproduction in any medium, provided the original work is properly cited.

Accurate estimation of vehicle states is extremely crucial for vehicle stability control. As a reliable estimation methodology, the unscented Kalman filter (UKF) has been widely utilized in vehicle control. However, the estimation accuracy still needs to be improved caused by the unpredictable measurement and process noise. In this paper, a novel modified UKF state estimation methodology combined with the ant lion optimization (ALO) is proposed for the stability control of a four in-wheel motor independent drive electric vehicle (4WIDEV). First, the optimal performance of the ALO algorithm is analyzed, where both unimodal and multimodal optimization test functions are selected and optimized by GA, PSO, and ALO, respectively. The results indicate that the ALO algorithm has good global optimization capability and applicability. Second, the ALO algorithm is merged into the UKF to adjust the statistical properties of noise information for the ALOUKF estimator design without extra sensor signals. At last, the simulations on the Matlab/Simulink-CarSim co-simulation platform and the road test based on an A&D 5435 rapid prototyping experiment platform (RPP) are carried out to verify the proposed method. The simulation and experiment results demonstrate that the ALOUKF estimator can improve state estimation accuracy and resist the vehicle nonlinearity even in the case of the complicated and emergency maneuvers.

1. Introduction

With the development of the automobile industry, the four in-wheel motor independent drive electric vehicles (4WIDEVs) have attracted increasing attention due to their contribution to energy saving and environmental protection [1–3]. Moreover, the 4WIDEV has a lot of advantages compared with the centralized drive electric vehicles (CDEVs) [4], where the independent control of each wheel is of great benefit for the improvement of the vehicle stability control [5]. Currently, different kinds of vehicle stability control systems have been developed to improve vehicle handling stability and driving safety. The well-known vehicle stability control technologies include the antilock braking system (ABS) [6], direct yaw moment control (DYC) [7], and active front steering (AFS) [8]. Most of them heavily depend on the knowledge of vehicle states for promoting vehicle stability control performance [9–11]. Generally speaking, the vehicle states used for vehicle stability control

are mainly composed of the side slip angle, yaw rate, tire-road force, and so on. Yaw rate can be directly measured by the micro-electromechanical system (MEMS) gyroscope [12], and side slip angle can be obtained from the optical sensors or Differential Global Positioning System (DGPS) [13]. However, these direct measurement methods are prohibitively expensive for the practical applications of ordinary vehicles. Therefore, it is necessary to develop an accurate and reliable methodology to estimate the vehicle states based on the onboard ordinary sensors.

A large number of research studies have been conducted in the field of vehicle state estimation. The state estimation methodologies can be mainly classified into two categories: kinematic and dynamic model-based methods. According to the kinematic equations between the vehicle acceleration, velocity, and yaw rate, the kinematic model-based method is established to estimate the vehicle states which is difficult to be measured. The key advantage of this method is its independence from the road condition and vehicle parameters

[14,15]. However, the acceleration, vehicle velocity, and yaw rate need to be measured by the onboard sensors; therefore, the decline of estimation accuracy is inevitable due to the sensor errors and unknown measurement noise. Bevely et al. developed a state estimation methodology by combining the inertial navigation system (INS) with a single antenna GPS; however, the roll and pitch motions were ignored [16]. Ryu et al. took into account the influence of roll and pitch motion to achieve accurate estimation of vehicle states and alleviate the sensor bias [17,18]. Selmanaj et al. discussed a side slip angle estimation approach without the knowledge of the tire-road friction and vehicle parameters. A heuristic stabilization term was introduced to integrate the kinematic model with empirical information which can guarantee the estimation performance during straight driving [19]. Based on previous research studies, to enhance the estimator accuracy, Selmanaj et al. improved the side slip angle estimator, where the roll angle was estimated to compensate for the effects of the acceleration measurement caused by gravity acceleration and vehicle roll [20]. But the road banks and inclination were not considered. Considering the influences of road banks and gradient on the estimation accuracy, Marco et al. proposed a multimodel sensor fusion estimation scheme combining a kinematic model with a dynamic model. Based on the information provided by a six-dimensional IMU and ESC sensors, the three-dimensional vehicle velocity, pitch, and roll angle were estimated [21].

Dynamic model-based methods usually use filter or observer technologies to estimate vehicle state. The commonly used vehicle state observers include sliding mode observer, robust observer, fuzzy observer, and so on. The nonlinear Kalman filter has been popularly utilized to address the state estimation problems [22], such as the extended Kalman filter (EKF) [23–25], unscented Kalman filter (UKF) [26–29], and their ramification [30,31]. Compared with the observer-based approach, the UKF has good robustness against sensor errors [20]. Baffet et al. designed a state estimator with two blocks. In the first block, a sliding model observer was established to calculate the tire-road forces. In the second block, the side slip angle and cornering stiffness were estimated by adopting the EKF algorithm. Moreover, an adaptive mechanism was introduced into EKF to coping with the variations in cornering stiffness [23,24]. Li et al. presented a novel multisensor fusion estimator combining the dynamic-based and kinematics-based methodologies. Two parallel EKF filters were designed to acquire the side slip angle and yaw rate. And a kinematics-based global federated estimator was used to realize the global fusion of inertial sensors [25]. This fusion estimator has a high estimation accuracy due to it has the superiority of both kinematic model-based and dynamic model-based. However, the EKF employs the linear operation of Taylor expansion, which will lead to the degradation of estimation accuracy, especially for the seriously nonlinear system. Besides, the Jacobian matrix is difficult to calculate.

As an improvement of EKF, UKF can address these issues. Due to the usage of the unscented transform (UT) to realize the nonlinear propagation of state error covariance, UKF has higher filtering precision and less computation complexity

[26]. Thus, it is more suitable for applications in the strong nonlinear dynamics systems. Jin and Yin combined the interacting multiple model (IMM) strategy with UKF and introduced a linear tire model and the nonlinear tire model, respectively, for the estimator design. The simulation results indicated that the proposed estimator can provide more reliable and accurate estimations compared with the IMMEKF estimator [28]. Heidfeld et al. designed an AUKF estimator to enhance the estimation accuracy of lateral velocity and tire slip, where a tire force adaption scheme was utilized to improve filter stability [29]. In the aforementioned research studies, the nonlinear system noise (measurement noise and process noise) in the process of UKF is generally assumed to be constant or selected by the trial-and-error method. However, the statistical characteristics of measurement noise and process noise are always unknown. Theoretically speaking, the measurement noise is determined by the precision of the onboard sensor. The prior can be obtained from the onboard sensor specifications. The process noise is determined by the system characteristic. It can be selected by contrast tests. But these methods are difficult to get the optimal values and are time-consuming. Thus, a lot of identifying noise approaches have been studied. Soken and Hajiyevev put forward a novel UKF algorithm based on the correction of process noise covariance [31]. Chen et al. introduced a square root cubature Kalman filter into the vehicle state estimator, in which the moving window method was used to adjust the covariance of measurement noise to improve the estimation accuracy and reliability [32]. However, the measurement noise and process noise were not obtained simultaneously. Wang et al. analyzed the relationship between the process noise and measurement noise under different road classifications. Based on the road classification, the process noise and measurement noise were both tuned [33].

Although the UKF estimator has been widely researched for vehicle applications, some drawbacks still exist due to the unknown system noise. The estimation performance of UKF can be further improved when the statistical characteristics of system noise are known. Motivated by the above review, this paper focuses on developing a novel vehicle state estimation methodology combining the UKF with the ant lion optimization (ALO). As a novel nature-inspired meta-heuristic algorithm, the ALO algorithm has been widely applied and vindicated to solve various optimization and identification problems [34–39]. It was utilized to optimize the allocation and sizing of renewable distributed generation sources in various distribution networks, where it had better performance in reducing power losses and improving energy saving [34]. An improved ALO algorithm was further proposed to parameter identification for the hydraulic turbine governing system, and the simulation results indicated that the ALO algorithm had good convergence characteristics and high stability [35]. Therefore, the core innovative idea of the proposed method is to embed the ALO algorithm into the UKF to adjust the statistical characteristics of process noise and measurement noise.

Firstly, based on the available measurement sensor signals, the 3-DOF vehicle dynamics model and nonlinear tire model are deduced and established for the estimator design. Due to the independent driving attribute of

4WIDEV, the wheel rotational dynamic model is built to calculate the tire-road longitudinal force. Secondly, the optimization performance of ALO algorithm is analyzed by using both unimodal and multimodal optimization test functions compared with the GA and PSO algorithms. According to the principle of the ALO algorithm, the system noise is regarded as the antlion position, and the fitness function is built to make the estimation error minimum. Then, the ALOUKF estimator is designed to estimate vehicle states without extra sensor measurements. Meanwhile, the process noise and measurement noise can be globally optimized simultaneously. Because the noise information is obtained based on the estimation and measurement data, it is the best for the nonlinear vehicle system and driving environment at present. Finally, the vehicle state estimation performance and accuracy can be improved due to the identification of the system noise.

The remaining of this paper is organized as follows. The correlation mathematical models are introduced and the UKF estimator is designed in Section 2. The principle of the ALO algorithm is described, and the algorithm performance is confirmed for the ALOUKF estimator design in Section 3. The state-space model is established, and the ALOUKF estimator performance is verified in the Matlab/Simulink-CarSim co-simulation platform and the rapid prototyping platform, respectively, and the detailed simulation and

experiment results and discussions are provided in Section 4 followed by the conclusions in Section 5.

2. Vehicle State Estimation Based on the UKF Algorithm

2.1. Correlation Models for Estimator Design

2.1.1. Vehicle Dynamics Model. The vehicle dynamics model with three degrees of freedom (3-DOF) is adopted for the estimation model establishment. The schematic diagram of the 3-DOF vehicle dynamics model is demonstrated in Figure 1, which involves the longitudinal, lateral, and yaw motions. The assumption here is that the pitch, roll, and vertical motions will not be considered, and the road irregularity and aerodynamics are neglected. The XGY coordinate represents global coordinate system. The xoy coordinate is vehicle coordinate system. The origin of xoy coordinate coincides with the vehicle gravity center. The x -axis signifies the longitudinal axis of the vehicle and forward is the positive direction, the y -axis indicates the lateral axis of the vehicle, and from right to left is the positive direction.

Based on the 3-DOF vehicle dynamics model and Newton's second law, the dynamic equations of the longitudinal, lateral, and yaw movements can be described as follows:

$$\begin{aligned} \sum F_x &= ma_x = m(\dot{v}_x - v_y\gamma) = (F_{xfl} + F_{xfr})\cos\delta + F_{xrl} + F_{xrr} - (F_{yfl} + F_{yfr})\sin\delta, \\ \sum F_y &= ma_y = m(\dot{v}_y + v_x\gamma) = (F_{xfl} + F_{xfr})\sin\delta + F_{yrl} + F_{yrr} + (F_{yfl} + F_{yfr})\cos\delta, \\ \sum M_z &= I_z\dot{\gamma} = (F_{xfl} + F_{xfr})a\sin\delta + (F_{yfl} + F_{yfr})a\cos\delta - (F_{yrl} + F_{yrr})b \\ &\quad - (F_{xfl} - F_{xfr})\frac{B_w}{2}\cos\delta - (F_{xrl} - F_{xrr})\frac{B_w}{2} + (F_{yfl} - F_{yfr})\frac{B_w}{2}\sin\delta, \end{aligned} \quad (1)$$

where M_z is the yaw moment, F_x and F_y are the longitudinal and lateral resultant force, respectively, m indicates the vehicle mass, a_x represents the longitudinal acceleration, a_y denotes the lateral acceleration, v_x and v_y indicate the longitudinal and lateral velocity, respectively, γ represents the vehicle yaw rate, I_z represents the inertia moment about the vertical axis, a and b are the distances from the vehicle gravity center to the front and rear axles, respectively, l is the wheel base, B_w is the wheel track, δ is the steering angle of the front wheels with the assumption that the steering angles of the front left and right wheels are the same, and F_{yij} and F_{xij} represent the lateral and longitudinal forces of each wheel, respectively. The subscript "ij" ($ij = fl, fr, rl, rr$) represents the specific wheel, fl is front left, fr is front right, rl is rear left, and rr is rear right. β denotes the side slip angle, which is defined as the angle between the vehicle speed direction and the vehicle longitudinal axis and can be calculated as follows:

$$\beta = \arctan \frac{v_y}{v_x}. \quad (2)$$

The relationship between the yaw rate and side slip angle is as follows:

$$\psi = \beta + \int \gamma dt, \quad (3)$$

where the ψ is course angle, which is the sum of side slip angle and yaw angle, and the yaw angle can be calculated by the time integration of the yaw rate.

2.1.2. Wheel Rotational Dynamic Model. The wheel rotational dynamic model is exhibited in Figure 2; different from the CDEV, each wheel of the 4WIDEV can be actuated independently by a hub motor. Thus, the driving/braking torque and wheel speed of each wheel can be derived from the signals of the motor actuator. Combining with these signals, the longitudinal tire-road force of each wheel can be calculated based on the rotational dynamic equation as follows:

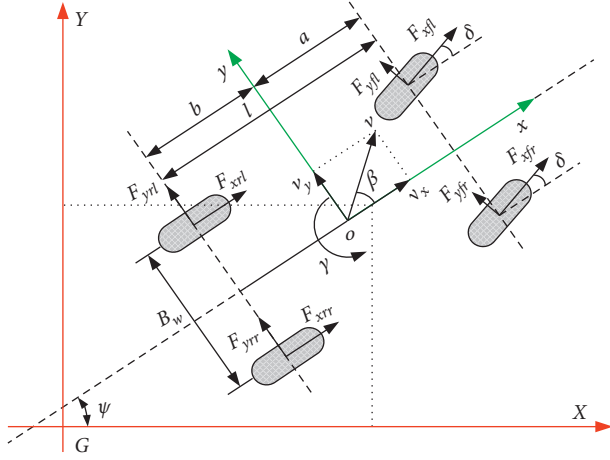


FIGURE 1: 3-DOF vehicle dynamics model.

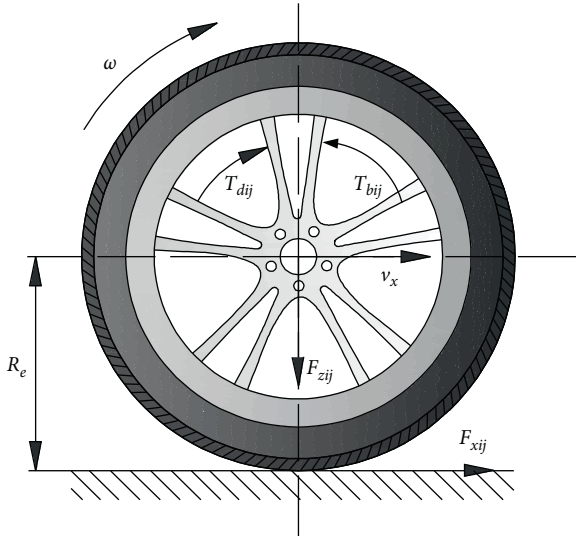


FIGURE 2: Wheel rotational dynamic model.

$$J_\omega \dot{\omega}_{ij} = T_{dij} - T_{bij} - F_{xij} R_e, \quad (4)$$

where J_ω is the wheel inertia moment to the rotary axis, R_e stands for the wheel effective rolling radius, ω_{ij} is the angular speed of each wheel, and T_{dij} and T_{bij} are the driving and brake torques of each wheel motor, respectively.

2.1.3. Tire Model. The vehicle motion is determined by the tire forces. Therefore, it is important to build an accurate tire model to describe the tire dynamic characteristic of the estimator design. The most commonly used tire models include the Pacejka tire model, the Dugoff tire model, and the Fiala tire model. The Dugoff tire model is a supplement to the elastic foundation analytical tire model developed by Fiala and the combined lateral-longitudinal force generation proposed by Pacejka; it provides a tire force calculation method for the combination of lateral and longitudinal tire force [40]. In this paper, the Dugoff nonlinear tire model is selected to build the estimation model of the lateral tire

force, and the mechanical characteristic of four wheels is assumed identical.

The lateral and longitudinal tire forces of each wheel can be expressed as follows:

$$\begin{cases} F_{xij} = C_{xij} \frac{s_{ij}}{1 - s_{ij}} f(L), \\ F_{yij} = C_{yij} \frac{\tan \alpha_{ij}}{1 - s_{ij}} f(L), \end{cases} \quad (5)$$

$$f(L) = \begin{cases} L(2 - L), & L < 1, \\ 1, & L \geq 1, \end{cases}$$

$$L = \frac{\mu_{ij} F_{zij} (1 - s_{ij})}{2 \sqrt{C_{xij}^2 \cdot s_{ij}^2 + C_{yij}^2 \cdot \tan^2 \alpha_{ij}}},$$

where F_{zij} is the vertical load of each wheel, C_{xij} is the longitudinal stiffness of each wheel, C_{yij} denotes the cornering stiffness of each wheel, μ_{ij} represents the road adhesion coefficient of each wheel (in this paper, the road adhesion coefficient of each wheel is assumed to equal and known), s_{ij} denotes the longitudinal slip ratio of each wheel, and α_{ij} represents the side slip angle of each wheel, which can be calculated as follows:

$$\begin{cases} \alpha_{fl,fr} = \arctan\left(\frac{v_y + a\gamma}{v_x \mp (B_w/2)\gamma}\right) - \delta, \\ \alpha_{rl,rr} = \arctan\left(\frac{v_y - b\gamma}{v_x \mp (B_w/2)\gamma}\right). \end{cases} \quad (6)$$

The longitudinal slip ratio of each wheel can be obtained as follows:

$$s_{ij} = \begin{cases} \frac{R_e \omega_{ij} - v_{wxij}}{r_e \omega_{ij}}, & R_e \omega_{ij} \geq v_{wxij}, \text{ driving,} \\ \frac{v_{wxij} - R_e \omega_{ij}}{v_{wxij}}, & R_e \omega_{ij} < v_{wxij}, \text{ braking,} \end{cases} \quad (7)$$

where v_{wxij} represents the wheel center speed.

The aforementioned Dugoff tire model is a quasisteady model, which ignores the transient characteristics of the tire. Therefore, to improve the tire model accuracy in the non-linear domain, the relaxation length is incorporated to indicate the transient characteristics of the tire, which is defined as the distance when the tire reaches a certain percentage of the steady-state condition under the stepwise change of slip angle [41,42]:

$$\begin{cases} \dot{F}_{yij} = \frac{v_c}{\sigma_{ij}} (-F_{yij} + \bar{F}_{yij}), \\ \dot{F}_{xij} = \frac{v_c}{\sigma_{ij}} (-F_{xij} + \bar{F}_{xij}), \end{cases} \quad (8)$$

where \bar{F}_{xij} and \bar{F}_{yij} represent the quasisteady longitudinal and the lateral tire forces of each wheel, respectively, σ_{ij} represents the relaxation length of each wheel, and v_c is the velocity of the center of vehicle mass.

Since the tire-road forces will be influenced by the redistribution of vertical load among four wheels during vehicle acceleration and turning, the knowledge of vertical tire forces is significant for the tire-road lateral forces estimation. With the consideration of the load transfer, the vertical load of each wheel can be calculated as follows:

$$\begin{cases} F_{zfl,fr} = b \left(\frac{mg}{2l} \mp \frac{ma_y h_g}{lB_w} \right) - \frac{ma_x h_g}{2l}, \\ F_{zrl,rr} = a \left(\frac{mg}{2l} \mp \frac{ma_y h_g}{lB_w} \right) + \frac{ma_x h_g}{2l}, \end{cases} \quad (9)$$

where h_g is the height of the gravity center.

2.2. The UKF Estimator Design. The most distinguished feature of UKF is its ability to deal with nonlinear problems by using the unscented transformation (UT) technology. The UT operation can generate a set of sigma points, which can represent the whole probability distribution. And the mean and covariance of sigma points are equal to the original state distribution. Therefore, the UKF algorithm is more appropriate for the state estimation of the nonlinear vehicle dynamics system.

The basic discrete-time equations of nonlinear stochastic system model are given by

$$\begin{cases} \mathbf{x}_{k+1} = f(\mathbf{x}_k, \mathbf{u}_k) + \mathbf{w}_k, \\ \mathbf{z}_k = h(\mathbf{x}_k, \mathbf{u}_k) + \mathbf{v}_k, \end{cases} \quad (10)$$

where k is the sampling instant, \mathbf{x} represents the state vector, \mathbf{u} denotes the input vector, \mathbf{z} is the measurement vector, and \mathbf{w} and \mathbf{v} signify the process noise and measurement noise, respectively. In this paper, the process noise and measurement noise are assumed irrelevant zero mean Gaussian noise with the covariance matrices expressed by \mathbf{Q} and \mathbf{R} . $\omega_k \sim N(0, \mathbf{Q}_k)$, $\mathbf{v}_k \sim N(0, \mathbf{R}_k)$. $f(\bullet)$ is the function of nonlinear state equation, and $h(\bullet)$ is the function of nonlinear observation equation.

The detailed state estimation procedure based on the UKF algorithm is described in Algorithm 1. The initial state and error covariance matrix are, respectively, obtained in step 1. In the time update step, the state at moment $k+1$ can be predicted based on the state at moment k . In the measurement update step, the estimation result can be corrected in combination with the measurable sensor information. \mathbf{P} is the error covariance matrix, and λ represents a scaling factor, where $\lambda = \zeta^2(n + \kappa) - n$, $\kappa = 0$. ζ represents the distribution of the sigma points around the state mean. ζ is usually set as a positive in the interval of $[1e-4, 1]$, where $\zeta = 1e-2$. τ is a nonnegative weight factor for incorporate the high order error. $\omega_i^{(m)}$, $\omega_i^{(c)}$ ($i=0, 1, 2, \dots, 2n$) represent the mean and covariance of the i -th sigma point, respectively. In the conventional UKF estimator, \mathbf{Q} and \mathbf{R} usually are set as constant matrices based on the empirical analysis.

Based on the aforementioned UKF framework, combining vehicle and tire dynamic models, the nonlinear state-space equations for vehicle state estimation can be rearranged as follows:

$$\begin{cases} \dot{v}_x = a_x + v_y \gamma = \frac{1}{m} [F_{xfl} \cos \delta - F_{yfl} \sin \delta + F_{xfr} \cos \delta - F_{yfr} \sin \delta + F_{xrl} + F_{xrr}] + v_y \gamma, \\ \dot{v}_y = a_y - v_x \gamma = \frac{1}{m} [F_{xfl} \sin \delta + F_{yfl} \cos \delta + F_{xfr} \sin \delta + F_{yfr} \cos \delta + F_{yrl} + F_{yrr}] - v_x \gamma, \\ \dot{\gamma} = \frac{1}{I_z} [(F_{xfl} + F_{xfr})a \sin \delta + (F_{yfl} + F_{yfr})a \cos \delta - (F_{yrl} + F_{yrr})b \\ - (F_{xfl} - F_{xfr})\frac{B_w}{2} \cos \delta - (F_{xrl} - F_{xrr})\frac{B_w}{2} + (F_{yfl} - F_{yfr})\frac{B_w}{2} \sin \delta], \\ \dot{F}_{yij} = \frac{v_c}{\sigma_{ij}} (-F_{yij} + \bar{F}_{yij}), \\ \dot{F}_{xij} = \frac{v_c}{\sigma_{ij}} (-F_{xij} + \bar{F}_{xij}). \end{cases} \quad (11)$$

According to the nonlinear vehicle state-space equation, the system state vector includes the longitudinal velocity,

lateral velocity, yaw rate, and tire-road lateral force of each wheel, which can be defined as follows:

Step 1: initialization ($k=0$)

$$\tilde{\mathbf{x}}_0 = E(\mathbf{x}_0)$$

$$\mathbf{P}_0 = E[(\mathbf{x}_0 - \tilde{\mathbf{x}}_0)(\mathbf{x}_0 - \tilde{\mathbf{x}}_0)^T]$$

Step 2: time update ($k=0,1,2, \dots$)

$$\text{Generate sigma points: } \begin{cases} \mathbf{x}_{i,k} = \tilde{\mathbf{x}}_k + (\sqrt{(n+\lambda)\mathbf{P}_k})_i, & i = 1 \sim n, \\ \mathbf{x}_{i,k} = \tilde{\mathbf{x}}_k - (\sqrt{(n+\lambda)\mathbf{P}_k})_i, & i = n+1, \dots, 2n \end{cases}$$

$$\text{Calculate sigma points' weight: } \omega_0^{(m)} = \lambda/(n+\lambda), \omega_0^{(c)} = \omega_0^{(m)} + (1 - \zeta^2 + \tau), \omega_i^{(m)} = \omega_i^{(c)}/2(n+\lambda), i = 1, 2, \dots, 2n$$

The step prediction of sigma points: $\mathbf{x}_{i,k+1|k} = f(\mathbf{x}_{i,k}, \mathbf{u}_k)$

$$\text{The state mean and error covariance matrix of step prediction: } \tilde{\mathbf{x}}_{k+1|k} = \sum_{i=0}^{2n} \omega_i^{(m)} \mathbf{x}_{i,k+1|k}, \mathbf{P}_{k+1|k} = \sum_{i=0}^{2n} \omega_i^{(c)} (\mathbf{x}_{i,k+1|k} - \tilde{\mathbf{x}}_{k+1|k})(\mathbf{x}_{i,k+1|k} - \tilde{\mathbf{x}}_{k+1|k})^T + \mathbf{Q}$$

$$\text{According to the step prediction, generate new sigma points: } \begin{cases} \mathbf{x}_{i,k+1|k} = \tilde{\mathbf{x}}_{k+1|k} + (\sqrt{(n+\lambda)\mathbf{P}_{k+1|k}})_i, & i = 1 \sim n \\ \mathbf{x}_{i,k+1|k} = \tilde{\mathbf{x}}_{k+1|k} - (\sqrt{(n+\lambda)\mathbf{P}_{k+1|k}})_i, & i = n+1, \dots, 2n \end{cases}$$

Step 3: measurement update ($k=0,1,2, \dots$)

Propagate the new sigma points by $h(\bullet)$, and the predicted observation is given by $\mathbf{z}_{i,k+1|k} = h(\mathbf{x}_{i,k+1|k}, \mathbf{u}_k)$

$$\text{The mean of system observation: } \hat{\mathbf{z}}_{k+1|k} = \sum_{i=0}^{2n} \omega_i^{(m)} \mathbf{z}_{i,k+1|k}$$

$$\text{The error covariance matrix of system observation: } \mathbf{P}_{z_k z_k} = \sum_{i=0}^{2n} \omega_i^{(c)} (\mathbf{z}_{i,k+1|k} - \hat{\mathbf{z}}_{k+1|k})(\mathbf{z}_{i,k+1|k} - \hat{\mathbf{z}}_{k+1|k})^T + \mathbf{R}$$

$$\text{Calculate the cross-correlation covariance matrix: } \mathbf{P}_{x_k z_k} = \sum_{i=0}^{2n} \omega_i^{(c)} (\mathbf{x}_{i,k+1|k} - \tilde{\mathbf{x}}_{k+1|k})(\mathbf{z}_{i,k+1|k} - \hat{\mathbf{z}}_{k+1|k})^T$$

$$\text{Calculate the Kalman filter feedback gain matrix: } \mathbf{K}_{k+1} = \mathbf{P}_{x_k z_k} \mathbf{P}_{z_k z_k}^{-1}$$

$$\text{The update of state estimation: } \hat{\mathbf{x}}_{k+1|k+1} = \hat{\mathbf{x}}_{k+1|k} + \mathbf{K}_{k+1} (\mathbf{z}_{k+1} - \hat{\mathbf{z}}_{k+1|k})$$

$$\text{The update of the error covariance matrix: } \mathbf{P}_{k+1|k+1} = \mathbf{P}_{k+1|k} - \mathbf{K}_{k+1} \mathbf{P}_{z_k z_k} \mathbf{K}_{k+1}^T$$

ALGORITHM 1: The state estimation procedure based on the UKF algorithm.

$$\begin{aligned} \mathbf{x} &= [x_1, x_2, x_3, x_4, x_5, x_6, x_7]^T \\ &= [v_x, v_y, \gamma, F_{yfl}, F_{yfr}, F_{yrl}, F_{yrr}]^T. \end{aligned} \quad (12)$$

The system measurement vector includes the yaw rate, longitudinal acceleration, and lateral acceleration is given by

$$\mathbf{z} = [z_1, z_2, z_3]^T = [\gamma, a_x, a_y]^T. \quad (13)$$

In this paper, it is assumed that the 4WIDEV has equipped with several ordinary off-the-shelf sensors. The longitudinal acceleration, lateral acceleration, and yaw rate

can be obtained by using an inertial navigation sensor. The steering wheel angle can be measured by a steering wheel angle sensor. The motor speed and torque can be received from the CAN signal of the motor controller. Therefore, the system input vector \mathbf{u} consists of the front wheel steering angle, and longitudinal tire force of each wheel is given by

$$\mathbf{u} = [u_1, u_2, u_3, u_4, u_5]^T = [\delta, F_{xfl}, F_{xfr}, F_{xrl}, F_{xrr}]^T. \quad (14)$$

The function $f(\bullet)$ of nonlinear state equation for vehicle state estimation can be rewritten as follows:

$$\begin{aligned} f(\cdot) &= [f_1, f_2, \dots, f_7]^T, \\ \left\{ \begin{aligned} f_1 &= \frac{1}{m} [u_2 \cos u_1 - x_4 \sin u_1 + u_3 \cos u_1 - x_5 \sin u_1 + u_4 + u_5] + x_2 x_3, \\ f_2 &= \frac{1}{m} [u_2 \sin u_1 + x_4 \cos u_1 + u_3 \sin u_1 + x_5 \cos u_1 + x_6 + x_7] - x_1 x_3, \\ f_3 &= \frac{1}{I_z} [(u_2 + u_3)a \sin u_1 + (x_4 + x_5)a \cos u_1 - (x_6 + x_7)b \\ &\quad - (u_2 - u_3) \frac{B_w}{2} \cos u_1 - (u_4 - u_5) \frac{B_w}{2} + (x_4 - x_5) \frac{B_w}{2} \sin u_1], \\ f_4 &= \frac{v_c}{\sigma} (-x_4 + \overline{F_{yfl}}), f_5 = \frac{v_c}{\sigma} (-x_5 + \overline{F_{yfr}}), \\ f_6 &= \frac{v_c}{\sigma} (-x_6 + \overline{F_{yrl}}), f_7 = \frac{v_c}{\sigma} (-x_7 + \overline{F_{yrr}}). \end{aligned} \right. \quad (15) \end{aligned}$$

The function $h(\bullet)$ of nonlinear observation equation for vehicle state estimation can be expressed as follows:

$$h(\cdot) = [h_1, h_2, h_3]^T,$$

$$\begin{cases} h_1 = x_3, \\ h_2 = \frac{1}{m} [u_2 \cos u_1 - x_4 \sin u_1 + u_3 \cos u_1 - x_5 \sin u_1 + u_4 + u_5], \\ h_3 = \frac{1}{m} [u_2 \sin u_1 + x_4 \cos u_1 + u_3 \sin u_1 + x_5 \cos u_1 + x_6 + x_7]. \end{cases} \quad (16)$$

Equation (11) is the nonlinear continuous-time form of the state-space equations, which needs to be transformed as a discrete-time form in the process of UKF; based on the difference method, the vehicle state estimation model is discretized and rewritten as

$$\begin{cases} v_{x,k+1} = \frac{T_s}{m} [F_{xfl,k} \cos \delta_k - F_{yfl,k} \sin \delta_k + F_{xfr,k} \cos \delta_k - F_{yfr,k} \sin \delta_k + F_{xrl,k} + F_{xrr,k}] + v_{y,k} \gamma_k, \\ v_{y,k+1} = \frac{T_s}{m} [F_{xfl,k} \sin \delta_k + F_{yfl,k} \cos \delta_k + F_{xfr,k} \sin \delta_k + F_{yfr,k} \cos \delta_k + F_{yrl,k} + F_{yrr,k}] - v_{x,k} \gamma_k, \\ \gamma_{k+1} = \frac{T_s}{I_z} [(F_{xfl,k} + F_{xfr,k})a \sin \delta_k + (F_{yfl,k} + F_{yfr,k})a \cos \delta_k - (F_{yrl,k} + F_{yrr,k})b \\ - (F_{xfl,k} - F_{xfr,k}) \frac{B_w}{2} \cos \delta_k - (F_{xrl,k} - F_{xrr,k}) \frac{B_w}{2} + (F_{yfl,k} - F_{yfr,k}) \frac{B_w}{2} \sin \delta_k], \\ F_{yij,k+1} = \frac{v_{c,k}}{\sigma_{ij,k}} (-F_{yij,k} + \overline{F}_{yij}), F_{xij,k+1} = \frac{v_{c,k}}{\sigma_{ij,k}} (-F_{xij,k} + \overline{F}_{xij}), \end{cases} \quad (17)$$

where T_s is the sampling time and set as 0.01 s in this paper.

Based on the above analysis, the nonlinear state-space model for vehicle state estimation is built for the UKF estimator design, and the side slip angle, yaw rate, and tire-road lateral force of each wheel can be estimated.

3. Vehicle State Estimation Based on a Modified UKF Algorithm

3.1. Introduction of ALO Algorithm. ALO is a novel optimization algorithm which was originally presented by Mirjalili; it imitates the predation behavior between antlion and ant to solve the optimization problems [37,39,43]. The flowchart of ALO is shown in Figure 3; the main operations of hunting include random walks of ants, entrapment in an antlion pit, building trap, catching prey, and rebuilding the pit. The details can be described as follows.

- (1) Random walks of ants: the ants move stochastically over the search space with random walks, which can be defined as

$$X(t) = [0, \text{cumsum}(2r(t_1) - 1), \text{cumsum}(2r(t_2) - 1), \dots, \text{cumsum}(2r(t_T) - 1)], \quad (18)$$

where cumsum is used to calculate the cumulative sum, T represents the maximum iterations, t

indicates the current iteration, and the stochastic function $r(\cdot)$ is given by

$$r(t) = \begin{cases} 1, & \text{if rand} > 0.5, \\ 0, & \text{if rand} \leq 0.5, \end{cases} \quad (19)$$

where rand is used to generate a random number in $[0, 1]$.

To keep the ants inside the search space which has a certain boundary, the random walks of ants should be normalized as follows:

$$X_i^t = \frac{(X_i^t - a_i) \times (d_i - c_i^t)}{(b_i^t - a_i)} + c_i^t, \quad (20)$$

where X_i^t is the position of random walk for i -th ant at t -th iteration, a_i and b_i are the minimum and maximum of random walk of i -th ant, respectively, and c_i^t and d_i^t indicate the minimum and maximum of i -th ant at t -th iteration, respectively.

- (2) Entrapment in an antlion pit: the random walks of ants are influenced by the traps of antlions. This can be modeled as follows:

$$\begin{cases} c_i^t = \text{Antlion}_j^t + c^t, \\ d_i^t = \text{Antlion}_j^t + d^t, \end{cases} \quad (21)$$

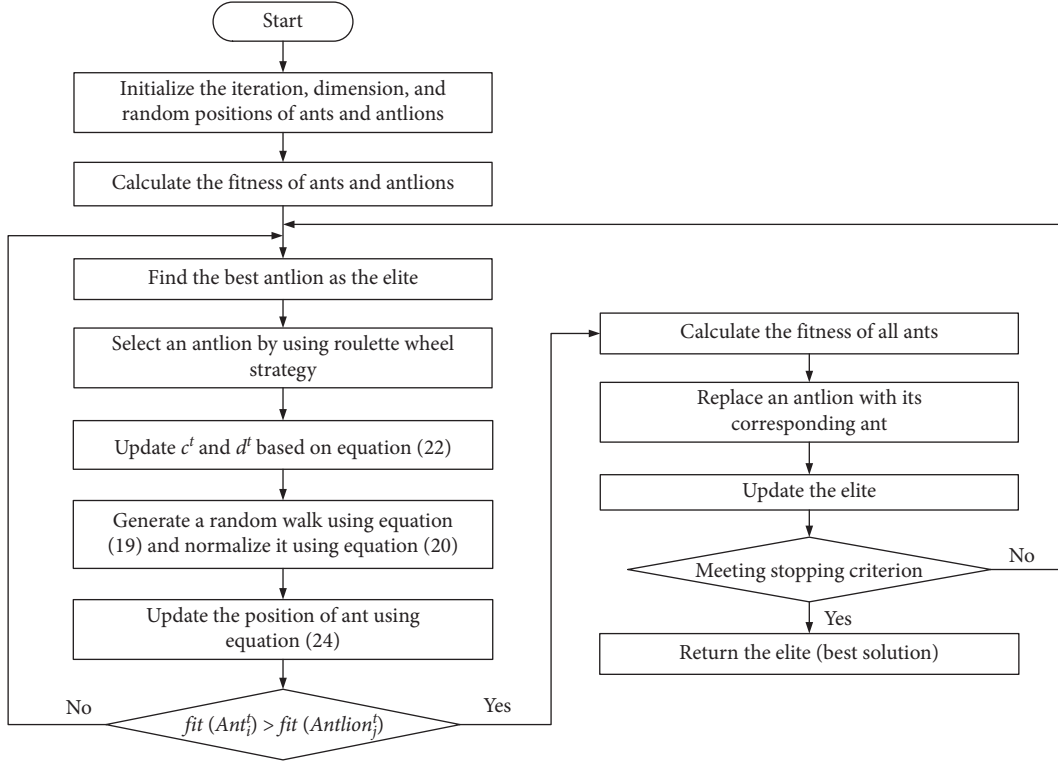


FIGURE 3: The flowchart of the ALO algorithm.

where c^t and d^t are the minimum and maximum of all ants at t -th iteration, respectively. Antlion_j^t represents the position of the selected j -th antlion at t -th iteration. Equation (21) demonstrates that the ants move within a hypersphere, which is determined by the c and d around a selected antlion.

- (3) Building trap: the roulette wheel strategy is utilized for selecting antlions based on their fitness. The size of antlion pit is in proportion to its fitness, and the larger pit has a higher probability of catching ants [44].
- (4) Sliding ant towards antlion: when the ant falls into the pit, the antlion will throw sands towards the slope of the cone shape to prevent the escape of ant. It means the radius of the hypersphere should be decreased adaptively as follows:

$$\begin{cases} c^t = \frac{c^t}{I}, \\ d^t = \frac{d^t}{I}, \end{cases} \quad (22)$$

$$\begin{cases} \rho = 2, & t > 0.1T, \\ \rho = 3, & t > 0.5T, \\ \rho = 4, & t > 0.75T, \\ \rho = 5, & t > 0.9T, \\ \rho = 6, & t > 0.95T, \end{cases}$$

where I is the ratio (here $I = 10^\rho (t/N)$) and ρ represents a constant dependent on the current iteration.

- (5) Catching prey and rebuilding the pit: the antlion position is replaced with its corresponding ant when the ant becomes fitter than the antlion, which can be mimicked as follows:

$$\text{Antlion}_j^t = \text{Ant}_i^t, \quad \text{if } \text{fit}(\text{Ant}_i^t) > \text{fit}(\text{Antlion}_j^t), \quad (23)$$

where Ant_i^t represents the position of the i -th ant at t -th iteration and $\text{fit}(\bullet)$ indicates the fitness function.

- (6) Elitism: at each step during the optimization process, the best antlion is saved as the elite. Therefore, the elite can influence the ants' movements, and each ant randomly walks both around a selected antlion and the elite. It can be described as

$$\text{Ant}_i^t = \frac{R_A^t + R_E^t}{2}, \quad (24)$$

where R_A^t is the random walk around the selected antlion at t -th iteration and R_E^t is the random walk around the elite at t -th iteration.

3.2. Performance Verification of ALO Algorithm. In order to verify the optimization performance of the ALO algorithm, five standard test functions (Schaffer, Griewank, Ackley, Branin, and Six-Hump Camelback) are utilized to evaluate

the optimization performance and compared with the common optimization algorithms, such as GA and PSO.

The expression and global optimal solution of each function are listed in Table 1. Schaffer is a unimodal function, and Griewank, Ackley, Branin, and Six-Hump Camelback are the multimodal functions [45]. Figure 4 shows the three-dimensional diagram of each function. As shown in Figure 4(a), Schaffer function includes many oscillations and peaks. As shown in Figure 4(b), Griewank function has many widespread local minima points, which are regularly distributed [46]. As shown in Figure 4(c), Ackley function has many local minima solutions around the global minima at the center. The characteristics of Griewank and Ackley functions pose a risk for optimization algorithms to be trapped in local minima [37]. Branin function has three global minima. The plot on the left of Figure 4(e) is the Six-Hump Camelback function within the $[-3, 3]$ domain. For easier observation of the function's key characteristics, the plot on the right shows only a part of this domain; it can be seen that Six-Hump Camelback function has six local minima, two of which are global.

The particular parameters of test functions are set as follows: the population number is 20 and the maximum iteration number is 500. The parameters of GA are as follows: the crossover rate is 0.5 and the mutation rate is 0.3. The parameters of PSO are as follows: the learning coefficient of the individual is the same as that of community, which is set as 0.5, the inertia weight is 0.08, and the varying range of particle updated velocity is $[-1, 1]$. The parameters of ALO are as follows: the number of ants and antlions is equal to the number of particles. In addition, three indicators are considered to evaluate the optimization performance: optimal value, convergence iteration, and convergence time. The optimal value is the global optimal solution searching by the optimization algorithm. The convergence iteration represents the corresponding iteration when the global optimal solution is found and kept stable. The convergence time denotes the time corresponding to the convergence iteration. For fair comparison, three optimization algorithms will be conducted 10 times independently. The average of three evaluation indicators after the 10 times circulation (Ave_optimal, Ave_iteration, and Ave_time) is demonstrated in Table 2.

As shown in Table 2, for Schaffer function, PSO and ALO both can find the global optimal solution. But GA cannot search the optimal value, and Ave_optimal is 0.0097. For Griewank function, which has a large number of local optimal points, PSO and ALO can find the global minimum by thorough search. However, GA cannot find the global minimum and is trapped early into the local minimum at the 26-th iteration. For Ackley function, PSO falls into the local optimal and cannot search the global optimal, and Ave_optimal is 0.0257. GA and ALO can find the global optimal solution finally. Although the three optimization algorithms all have good performance for Branin function, which has a few local optimal points, the optimization error of ALO is minimum, and Ave_optimal is 0.3979. For Six-Hump Camelback, GA cannot find the global minimum until the 326-th iteration, but ALO can find the global

optimal solution, and Ave_optimal is -1.0316 which is equal to the desired value and the estimation error is less than that of the PSO.

In conclusion, compared with the other two popular optimization algorithms (GA and PSO), for the unimodal function, ALO has the same optimization performance as PSO, for the multimodal function with a few local optimal points, the optimization error of ALO is minimum; for the multimodal function with a lot of local optimal points, ALO can jump the local optimal and find the global minimum. Therefore, the ALO has good global optimization capability and applicability in different optimization problems. In this paper, the 4WIDEV is a complicated strong nonlinear system, so it is feasible and effective to choose the ALO algorithm to adjust the statistical properties of system noise.

3.3. Combination of ALO with UKF Algorithms. In the UKF estimator, the measurement noise and process noise are zero mean Gaussian noise with the covariance matrices expressed by \mathbf{Q} and \mathbf{R} , which can be defined as a diagonal and positive one. As shown in equations (13) and (14), the nonlinear state-space model of vehicle state estimation includes seven state variables and three measurement variables, and thus \mathbf{Q} and \mathbf{R} can be defined as follows:

$$\begin{cases} \mathbf{Q} = \text{diag}(q_1, q_2, q_3, q_4, q_5, q_6, q_7), \\ \mathbf{R} = \text{diag}(r_1, r_2, r_3). \end{cases} \quad (25)$$

To combine the UKF with the ALO algorithm, the elements of the covariance matrices \mathbf{Q} and \mathbf{R} can be merged into a vector \mathbf{y} which is given by

$$\mathbf{y} = (q_1, q_2, q_3, q_4, q_5, q_6, q_7, r_1, r_2, r_3)^T. \quad (26)$$

According to the principle of the ALO algorithm, q and r are regarded as the antlion position to be optimized, then the fitness function can be constituted based on the objective of state estimation, and finally, \mathbf{Q} and \mathbf{R} can be globally optimized by using the ALO algorithm in a certain sampling window. To make the state estimation error minimum, the optimization objective function (fitness function) can be defined as the square sum of error between the actual measurements and their estimations. The corresponding weights of measurements are added to the objective function, which can be described as follows:

$$F(\hat{\mathbf{y}}_j^t) = \sum_{k=1}^M \sum_{i=1}^3 W_i [\mathbf{z}_{i,k} - \hat{\mathbf{z}}_{i,k}(\hat{\mathbf{y}}_j^t)]^2, \quad (27)$$

where i is the dimension of the measurement vector, $\mathbf{z}_{i,k}$ represents the actual measurement value, which includes the yaw rate, longitudinal acceleration, and lateral acceleration, $\hat{\mathbf{z}}_{i,k}(\hat{\mathbf{y}}_j^t)$ signifies the corresponding estimation value of j -th antlion at t -th iteration, M is the length of the sampling window, and W_i is the weight coefficient (here $W_1 = 0.2$, $W_2 = 0.3$, and $W_3 = 0.5$).

The scheme of the vehicle state estimation is shown in Figure 5, which mainly includes two parts: the measurement signal output and the ALOUKF estimator. In the

TABLE 1: The five test functions.

Function	Function expression	Range	Global optimal
Schaffer	$f(x) = 0.5 + ((\sin\sqrt{(x_1^2 - x_2^2)})^2 - 0.5)/(1 + 0.001(x_1^2 + x_2^2))^2$	$[-10, 10]$	$\min f(x) = f(0, 0) = 0$
Griewank	$f(x) = \sum_{i=1}^D (x_i^2/4000) - \prod_{i=1}^D \cos(x_i/\sqrt{i}) + 1$	$[-10, 10]$	$\min f(x) = f(0, \dots, 0) = 0$
Ackley	$f(x) = -20 \exp(-0.2\sqrt{(1/D)\sum_{i=1}^D x_i^2}) - \exp((1/D)\sum_{i=1}^D \cos(2\pi x_i)) + 20 + e$	$[-10, 10]$	$\min f(x) = f(0, \dots, 0) = 0$
Branin	$f(x) = (x_2 - (5.1/4\pi^2)x_1^2 + (5/\pi)x_1 - 6)^2 + 10(1 - (1/8\pi)\cos(x_1)) + 10$	$x_1 \in [-5, 10]$ $x_2 \in [0, 15]$	$x_{\min} = (-\pi, 12.275), (\pi, 2.275), (9.425, 2.475)$ $\min f(x) = 0.397887$
Six-Hump Camelback	$f(x) = 4x_1^2 - 2.1x_1^4 + (x_1^6/3) + x_1x_2 - 4x_2^2 + 4x_2^4$	$[-3, 3]$	$\min f(x) = 1.0316$ $x_{\min} = (0.0898, -0.7126), (-0.0898, 0.7126)$

Note: D is set to 2 in this paper.

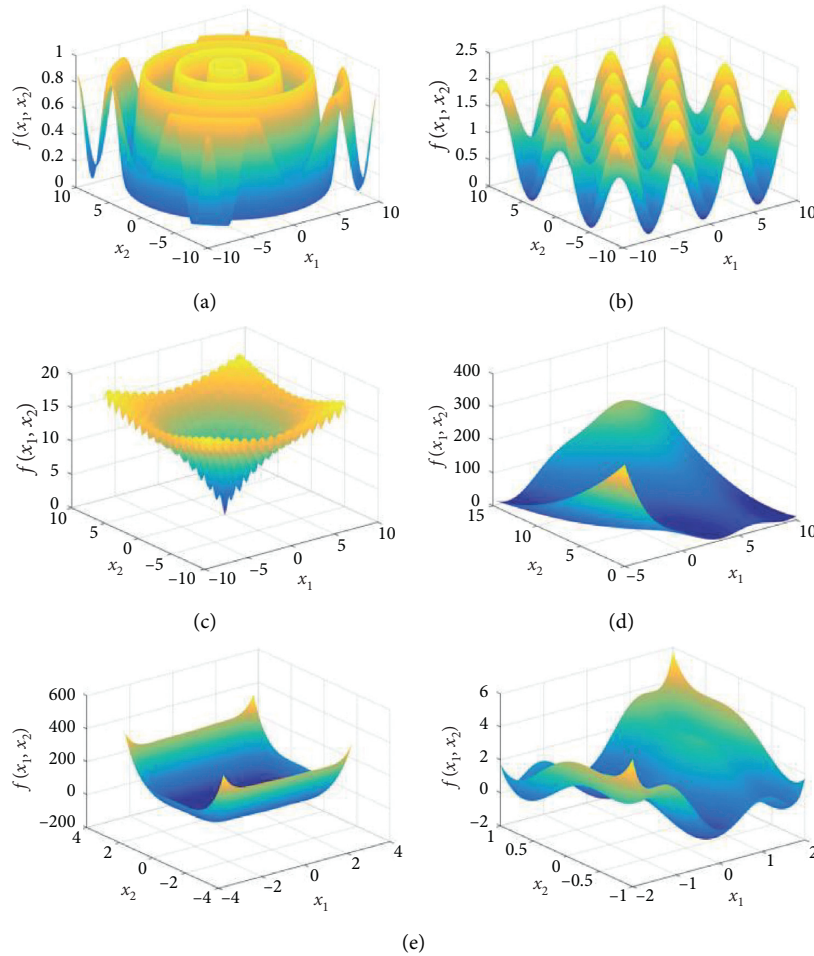


FIGURE 4: Three-dimensional diagram of test functions: (a) Schaffer; (b) Griewank; (c) Ackley; (d) Branin; (e) Six-Hump Camelback.

measurement signal output part, as we all know, the CarSim software can accurately simulate the dynamic behavior of passenger vehicles and has been extensively used in the development and verification of vehicle dynamics control systems. The foundational mathematical models representing the vehicle are sufficiently detailed and are of high

fidelity such that the simulation can replicate physically measured responses. According to the assumption in Section 2, 4WIDEV is equipped with several ordinary sensors, and a_x , a_y , δ , γ , and ω_{ij} can be regarded as measurable. Therefore, a_x , a_y , δ , and ω_{ij} generated from CarSim can represent the actual measurements and can be imported to the ALOUKF

TABLE 2: The optimization result comparison of different algorithms.

Function	Ave_optimal			Ave_iteration			Ave_time (s)		
	GA	PSO	ALO	GA	PSO	ALO	GA	PSO	ALO
Schaffer	0.0097	$5.9105e-06$	$7.5685e-06$	17	122	65	0.0118	0.0247	0.0870
Griewank	0.0074	$1.7831e-05$	$8.6813e-06$	26	367	267	0.0364	0.0756	0.3715
Ackley	$1.3126e-05$	0.0257	$2.9508e-06$	486	325	379	0.3187	0.0827	0.5073
Branin	0.3982	0.3985	0.3979	339	401	120	0.2495	0.0784	0.1554
Six-Hump Camelback	-1.0167	-1.0314	-1.0316	326	389	146	0.2269	0.0910	0.1878

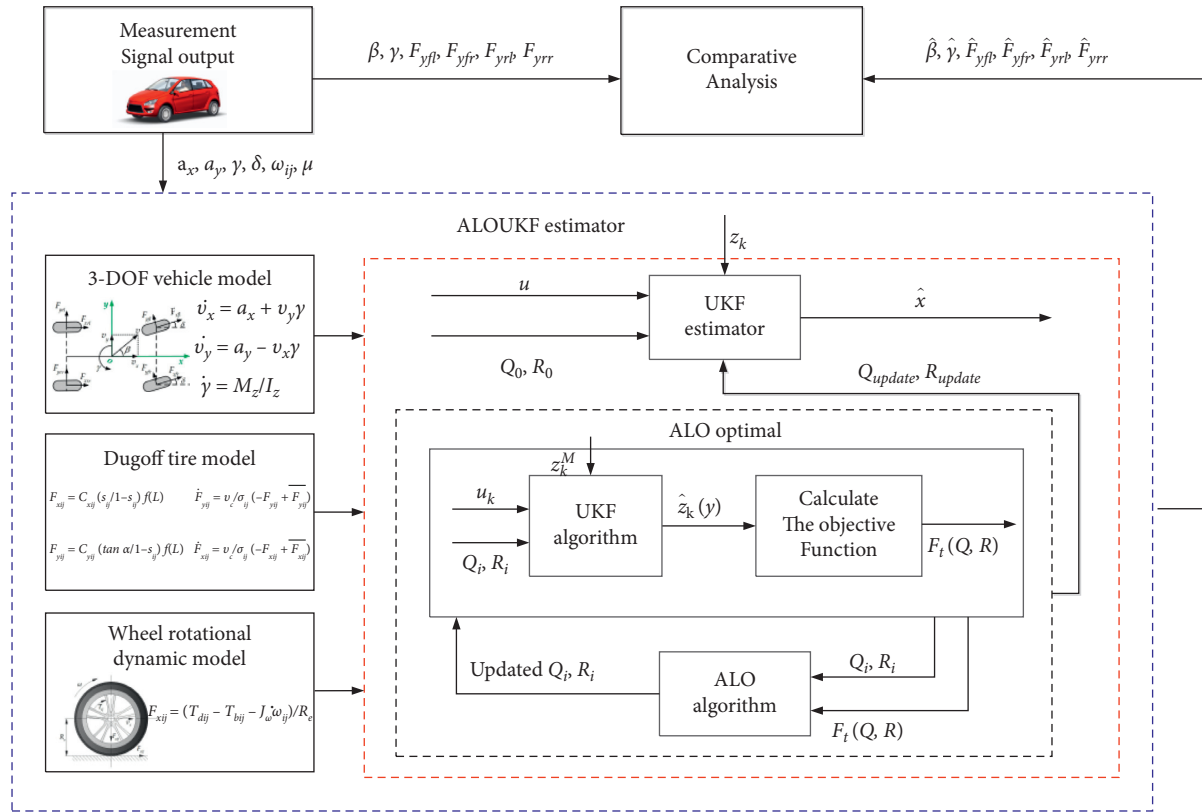


FIGURE 5: The scheme of the vehicle state estimation.

estimator for the state estimation model built. Besides, a_x , a_y , and γ generated from CarSim will be used to calculate the objective function, and $\hat{\beta}$, $\hat{\gamma}$, and F_{yij} output from CarSim will be taken for the reference value to compare with the estimation value.

The ALOUKF estimator with two modules is designed based on a modified UKF method, where the ALO algorithm is merged into it. In the upper module, the UKF estimator is designed and conducted to estimate vehicle states based on the measurements generated from CarSim. Meanwhile, in the ALO optimal module, the process noise and measurement noise can be integrated as an optimized vector, which represents the antlion positions. Based on the actual measurements of CarSim and their estimations in the window range, the ALO algorithm is applied to search the best \mathbf{Q} and \mathbf{R} to make the fitness minimum in the sampling window. Because the optimal \mathbf{Q} and \mathbf{R} are calculated based on the information in the

window range, the statistical characteristics of \mathbf{Q} and \mathbf{R} can be regarded as the best for the nonlinear vehicle system and driving environment at present. Once the updated \mathbf{Q} and \mathbf{R} are obtained from the ALO optimal module, the old \mathbf{Q} and \mathbf{R} will be replaced by the new value. Because the change amplitude of \mathbf{Q} and \mathbf{R} is relatively less than the vehicle state, before the optimal process is completed, the UKF estimator can still use the last updated \mathbf{Q} and \mathbf{R} for state estimation calculation. In this paper, the maximum iteration of the ALO algorithm is set as 400, the number of ants and antlions is set as 20, and the iteration is stopped when the fitness of the elite individual does not change in 10 continuous iterations. The length of the sampling window M is 200. At last, the ALOUKF estimator can realize the accurate estimation of the side slip angle, yaw rate, and tire-road lateral forces and the adjustment of the process noise and measurement noise simultaneously.

TABLE 3: Parameters of the vehicle (COG: center of gravity).

Parameters	Unit	Value
Total mass of vehicle	m/kg	840
Distance from COG to front wheels	a/m	1.21
Distance from COG to rear wheels	b/m	0.86
Wheel base	l/m	2.07
Wheel track	B_w/m	1.481
Tire model	—	165/65 R13
Wheel effective radius	R_e/m	0.272
Height of COG	h_g/m	0.68
Vehicle rotational inertia about z -axis	$I_z/(\text{kg}\cdot\text{m}^2)$	1523

4. Simulations and Experiment Results

4.1. Simulation Verification. Simulation tests will be carried out in the Matlab/Simulink-CarSim co-simulation platform to validate the effectiveness of the designed ALOUKF estimator and compare it with the EKF and UKF estimators. The vehicle dynamics model is provided by CarSim, and the wheel rotational dynamic model, the Dugoff tire model, and the ALOUKF estimator model are established in Simulink. The B-class hatchback vehicle model in CarSim is selected as the simulated vehicle. In order to reduce the model difference between the real vehicle and the simulation vehicle, the parameters for the B-class hatchback vehicle in CarSim are adjusted according to the test vehicle of the following road test. The particular geometric and inertial parameters of the vehicle are shown in Table 3. The severe double lane change and the complicated sine wave steering maneuvers are conducted, respectively. The maximum error (ME) and root mean square error (RMSE) are applied to quantitatively evaluate the estimation performance and can be calculated as follows:

$$\text{ME} = \max|\hat{\mathbf{x}}_{i,k} - \mathbf{x}_{i,k}|,$$

$$\text{RMSE} = \sqrt{\frac{1}{N} \sum_{k=1}^N \sum_{i=1}^7 (\hat{\mathbf{x}}_{i,k} - \mathbf{x}_{i,k})^2}, \quad (28)$$

where $\mathbf{x}_{i,k}$ represents the real measured values of vehicle state generated from CarSim and $\hat{\mathbf{x}}_{i,k}$ represents the estimation values of vehicle state obtained from the estimator.

4.1.1. Double Lane Change Maneuver. The severe double lane change maneuver specified in ISO 3888-1 is a standard test condition to verify vehicle stability, and the knowledge of vehicle states is crucial for the vehicle stability control system of 4WIDEV, so the severe double lane change maneuver under low road adhesion condition is conducted on a flat road. The initial speed is 60 km/h, and the road adhesion coefficient is 0.4. Figure 6 shows the steering wheel angle and the longitudinal velocity dynamic response.

Figure 7 shows the estimation result comparison of side slip angle and yaw rate between EKF, UKF, and ALOUKF estimators. The ME and RMSE for side slip angle and yaw rate are given in Table 4. As shown in Figure 7, the UKF and ALOUKF estimators both can satisfy the estimation

requirements in the straight driving stage; however, the estimation error of the EKF estimator is larger than that of the other two estimators through the whole simulation period since the linearization operation will lead to the increase of estimation error. As shown in the enlarged view of Figures 7(a) and 7(c), it is notable that the estimation deviations of side slip angle and yaw rate at the emergency turning are larger than those at the straight driving; this is because the vehicle state changes dramatically under the low adhesion road. Even so, the ALOUKF still outperforms others. It can be seen in Table 4 that the RMSE of side slip angle is improved by 41.21% and 53.26% compared with the UKF and EKF, respectively. The ME of side slip angle in ALOUKF estimator is 0.1447 deg, while that in UKF and EKF estimators is 0.2064 deg and 0.2745 deg, respectively. In Figure 7(c), EKF and UKF estimators both have a time lag between the estimated yaw rate and the real yaw rate generated from CarSim. However, the ALOUKF estimator can accurately track the real yaw rate, and the RMSE is only 0.1594 deg/s, which is less than that in EKF and UKF estimators.

Figure 8 shows the estimation result comparison of tire-road lateral force between the UKF and ALOUKF estimators; similar to the estimation results of side slip angle, UKF and ALOUKF estimators both perform well of estimating the tire-road lateral force on the straight road, but the estimation errors increase when the steering wheel angle changes suddenly. However, the increment of the ALOUKF estimator is less than that of UKF. Table 5 shows the comparison of ME and RMSE between UKF and ALOUKF; the ME of ALOUKF estimator is less than that of UKF, and the RMSE of tire-road lateral force for each wheel is decreased by 38.31%, 52.59%, 40.08%, and 46.68%, respectively.

This simulation confirms that the ALOUKF estimator has good estimation accuracy and trackability due to the adjustment of the measurement noise and process noise matrices.

4.1.2. Sine Wave Steering Maneuver. For further validation of the presented estimation method under drastic steering condition, the sine wave steering maneuver is carried out with an initial speed of 40 km/h and a road adhesion coefficient of 0.85. As shown in Figure 9(a), the steering wheel angle amplitude is 90 deg and the period is 4 s. Figure 9(b) shows the vehicle lateral acceleration. As shown in Figure 9, the steering wheel angle and lateral acceleration both have large and frequent fluctuations; meanwhile, all peak values of lateral acceleration are close to 0.4 g, and the maximum value reaches 0.4169 g. It means that the vehicle and tire are in a strong nonlinear state and are unstable.

Figure 10 shows the simulation results of side slip angle and yaw rate. The ME and RMSE comparison is listed in Table 6. As shown in Figure 10, the EKF estimator has a poor performance both in the estimation of side slip angle and yaw rate because the vehicle frequently goes into the nonlinear region. When the steering wheel angle changes gently, the estimation deviation of UKF and ALOUKF is small. When the steering wheel angle changes sharply, the estimation deviation of UKF increases

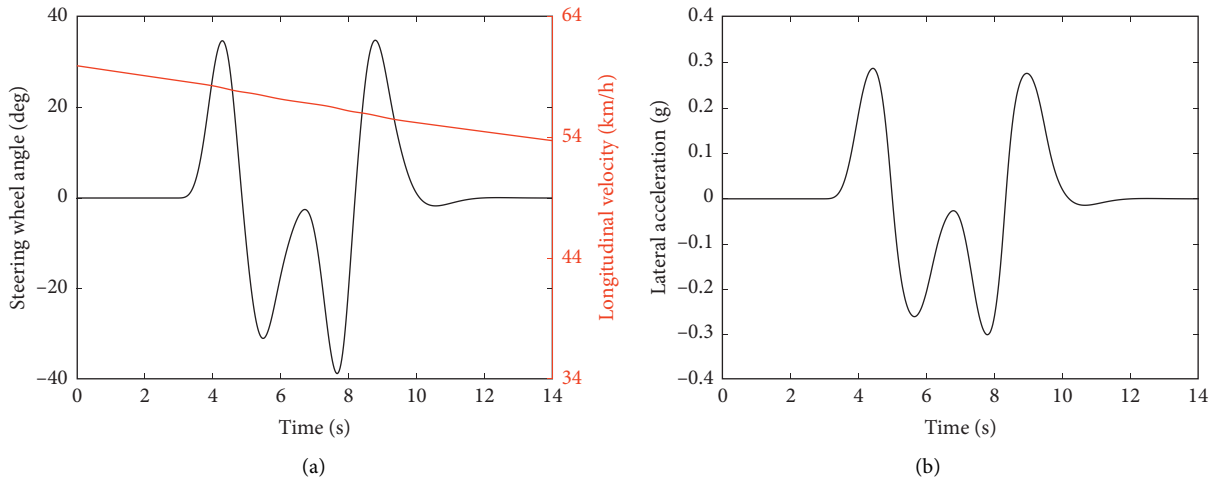


FIGURE 6: Vehicle state signals generated from CarSim: (a) steering wheel angle and longitudinal velocity; (b) lateral acceleration.

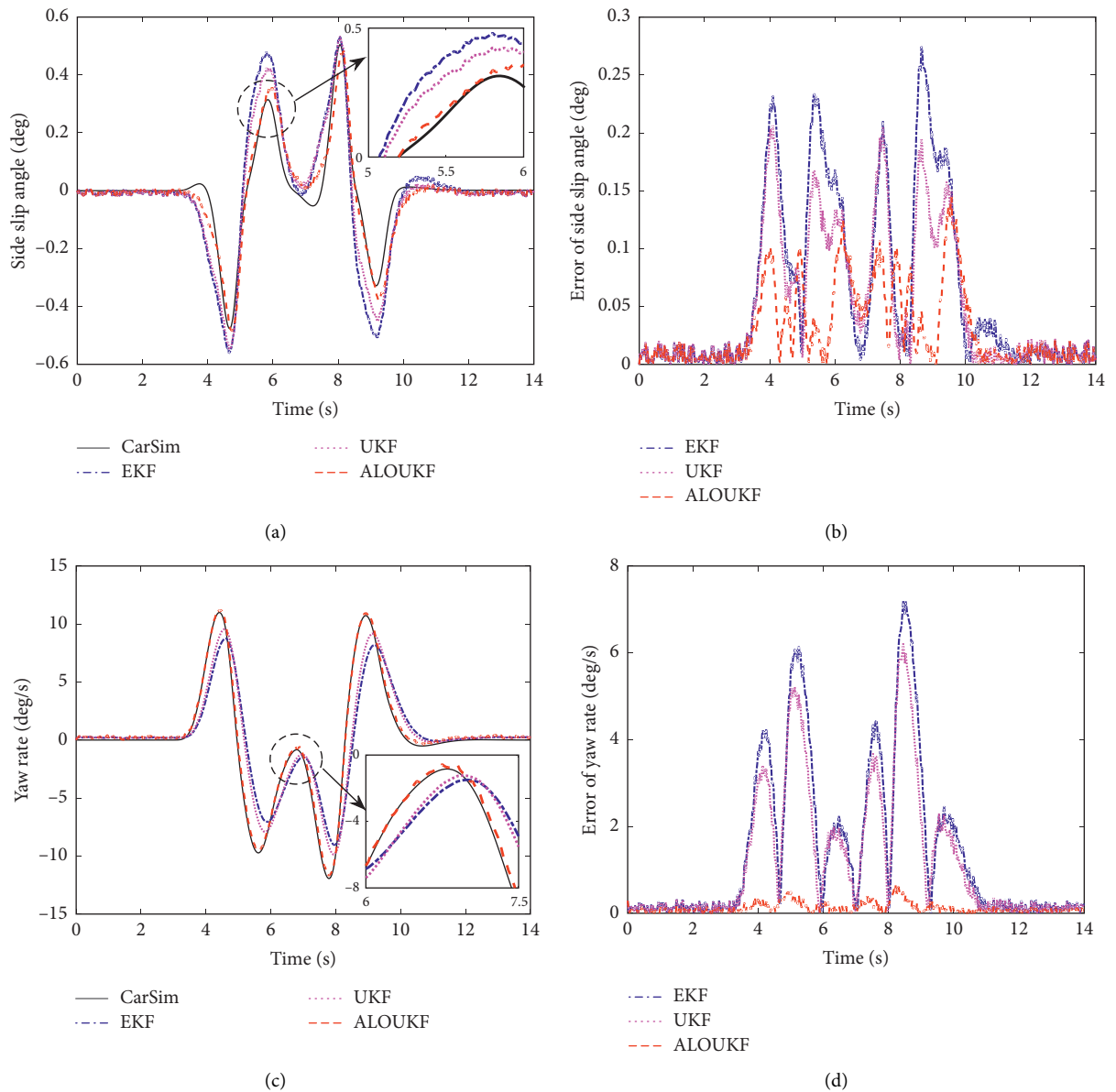


FIGURE 7: Simulation results of side slip angle and yaw rate for EKF, UKF, and ALOUKF estimators: (a) side slip angle; (b) error of side slip angle; (c) yaw rate; (d) error of yaw rate.

TABLE 4: Comparison of ME and RMSE for side slip angle and yaw rate.

State	ME			RMSE		
	EKF	UKF	ALOUKF	EKF	UKF	ALOUKF
γ (deg/s)	7.1879	6.2109	0.6841	2.2286	1.8430	0.1594
β (deg)	0.2745	0.2064	0.1447	0.0937	0.0745	0.0438

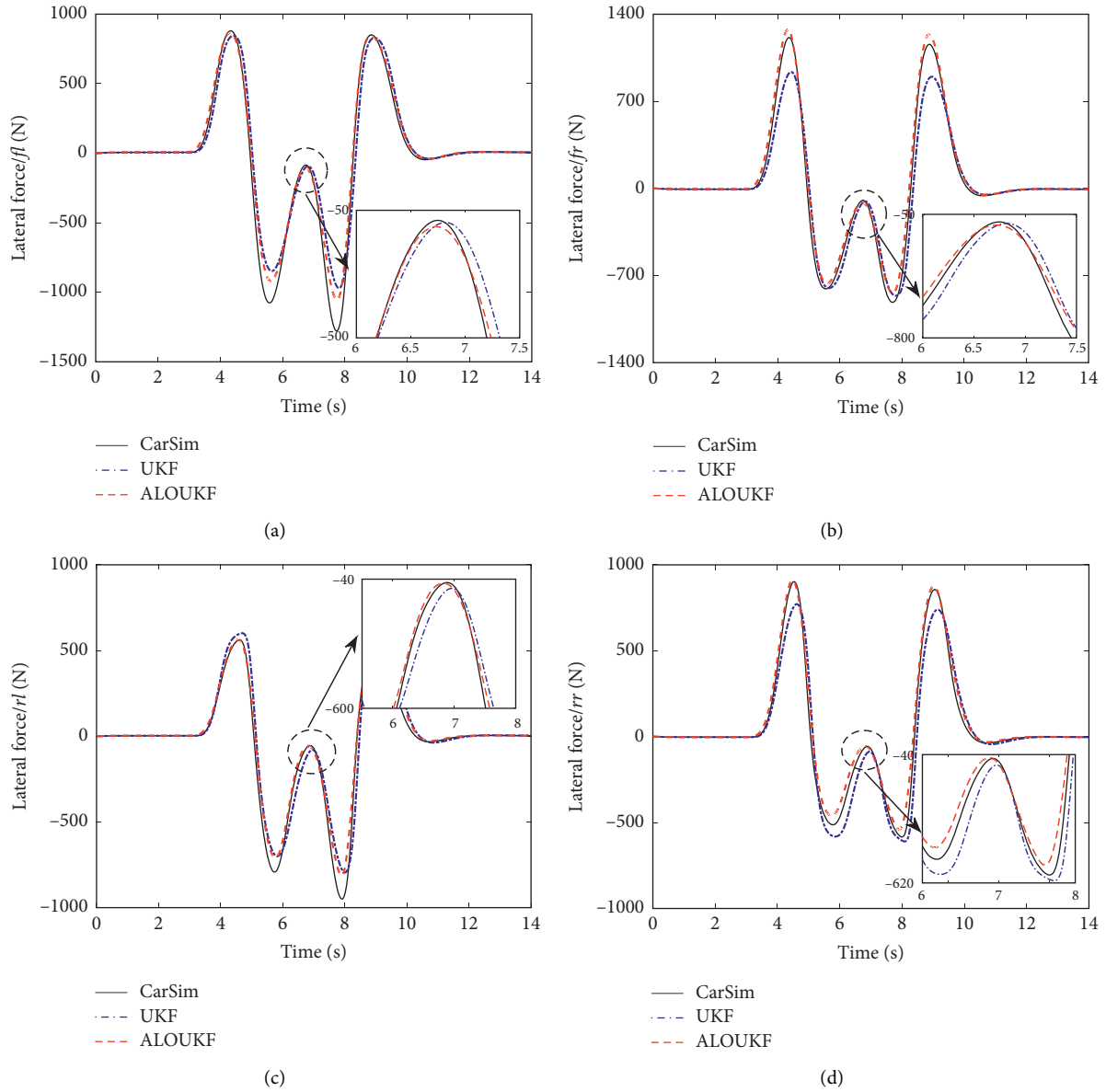


FIGURE 8: Simulation results of tire-road lateral force for UKF and ALOUKF estimators: (a) front left; (b) front right; (c) left rear; (d) right rear.

TABLE 5: Comparison of ME and RMSE for tire-road lateral force.

State (N)	ME		RMSE		RMSE improved (%)
	UKF	ALOUKF	UKF	ALOUKF	
F_{yfl}	345.3163	228.5535	105.9953	65.3919	38.31
F_{yfr}	309.0937	153.3153	106.5646	50.5215	52.59
F_{yrl}	262.2675	172.5306	73.4423	44.0059	40.08
F_{yrr}	226.4347	152.2261	72.7514	38.7920	46.68

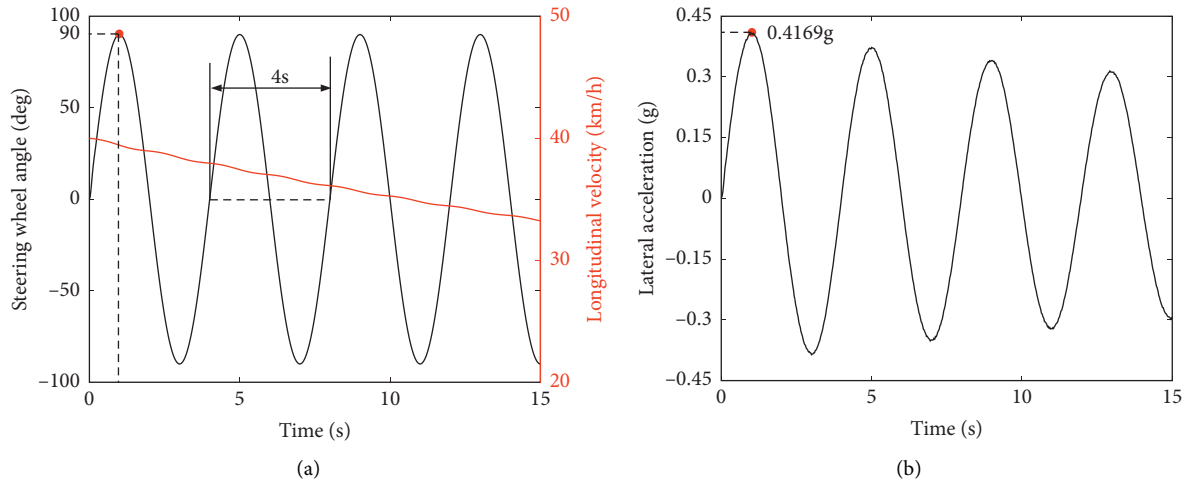


FIGURE 9: Vehicle state signals generated from CarSim: (a) steering wheel angle and longitudinal velocity; (b) lateral acceleration.

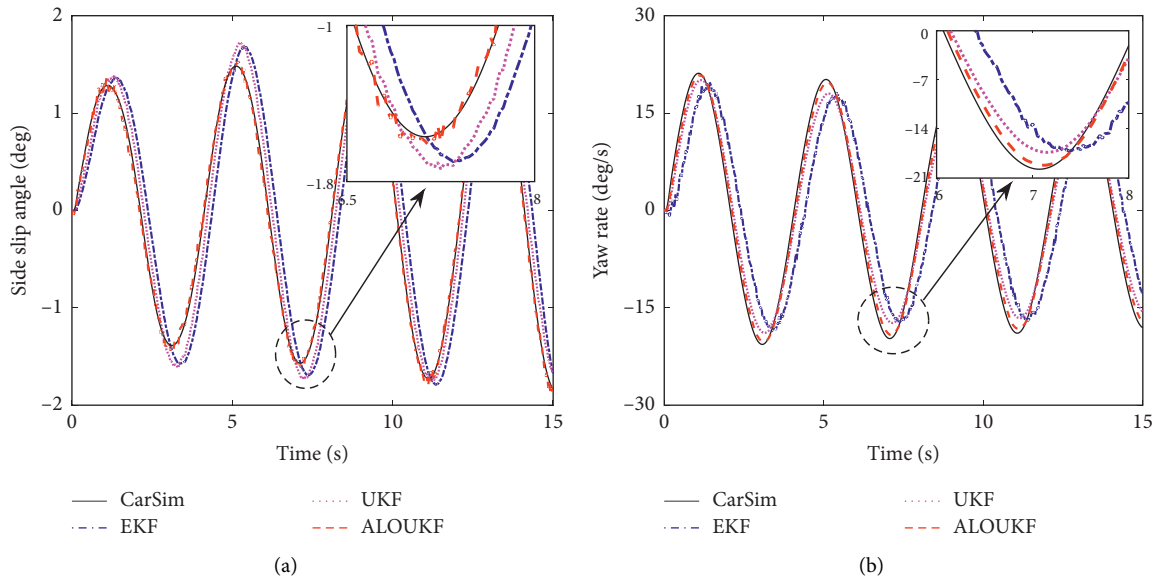


FIGURE 10: Simulation results of side slip angle and yaw rate for EKF, UKF, and ALOUKF estimators: (a) side slip angle; (b) yaw rate.

TABLE 6: Comparison of ME and RMSE for side slip angle and yaw rate.

State	ME			RMSE		
	EKF	UKF	ALOUKF	EKF	UKF	ALOUKF
γ (deg/s)	11.1912	3.4669	1.6873	6.9136	2.2211	1.0396
β (deg)	0.7163	0.3438	0.1930	0.4430	0.2150	0.0682

rapidly due to the vehicle nonlinearity, and the ME of yaw rate and side slip angle in UKF reaches 3.4669 deg/s and 0.3438 deg, respectively. But ALOUKF can still maintain the estimation error inside a small range and resist this dramatic fluctuation, and the ME of yaw rate and side slip angle is 1.6873 deg/s and 0.1930 deg, respectively.

Figure 11 shows the simulation comparison of tire-road lateral force between the UKF and ALOUKF estimators, and the estimation deviation of tire-road lateral forces is larger

than that under the double lane change maneuver due to the inevitable vehicle model error at the nonlinear region. But in general, the ALOUKF estimator performs better, especially in maximum steering wheel angle. As shown in Table 7, the RMSE of tire-road lateral force for each wheel is improved by 20.62%, 18.86%, 58.27%, and 52.70%, respectively. This simulation demonstrates that the proposed estimation method can accurately estimate vehicle state and resist the vehicle nonlinearity.

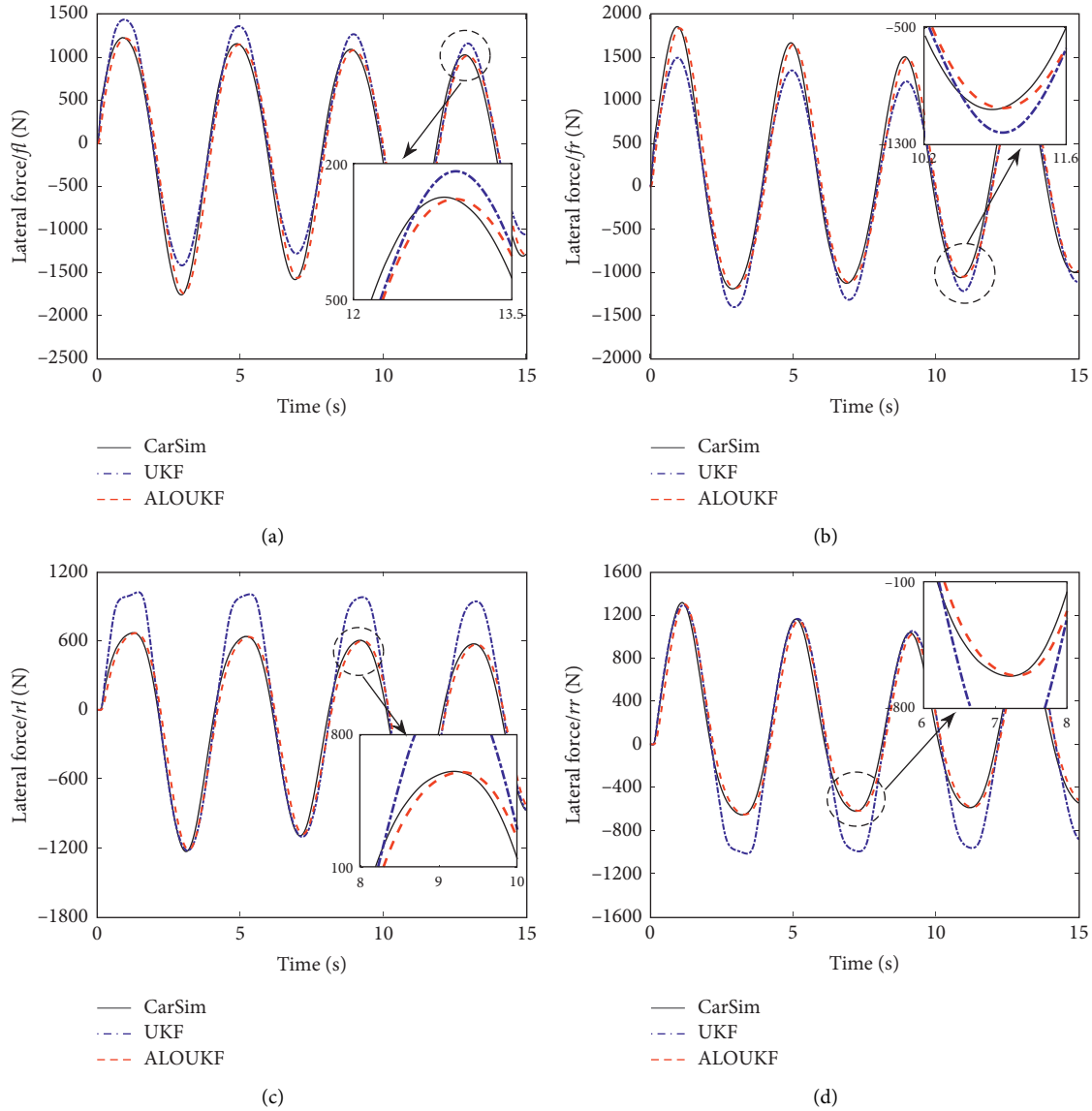


FIGURE 11: Simulation results of tire-road lateral force for UKF and ALOUKF estimators: (a) front left; (b) front right; (c) left rear; (d) right rear.

TABLE 7: Comparison of ME and RMSE for tire-road lateral force.

State (N)	ME		RMSE		RMSE improved (%)
	UKF	ALOUKF	UKF	ALOUKF	
F_{yfl}	345.3598	270.8882	181.8664	144.3570	20.62
F_{yfr}	362.9578	289.1788	183.1064	148.5645	18.86
F_{yrl}	395.9780	155.8817	220.7503	92.1301	58.27
F_{yrr}	396.0068	162.5478	202.8349	95.9343	52.70

4.2. Experiment Verification. The road test is conducted to further validate the feasibility of the proposed estimation method. A rapid prototyping platform (RPP) for 4WIDEV is established based on the A&D 5435 semiphysical simulation system and Matlab/Simulink code generation technology. The road test scene and the installed actual measuring sensors are shown in Figure 12. The configuration of the

4WIDEV test platform and the sensor signal transmission network are shown in Figure 13. A&D 5435 is applied to replace the vehicle controller and integrated into the Simulink Library interface module. Based on the Real-Time Workshop technology, the simulation model can be translated to C code to be loaded in the A&D 5435 and executed independently. The measurement signals input to

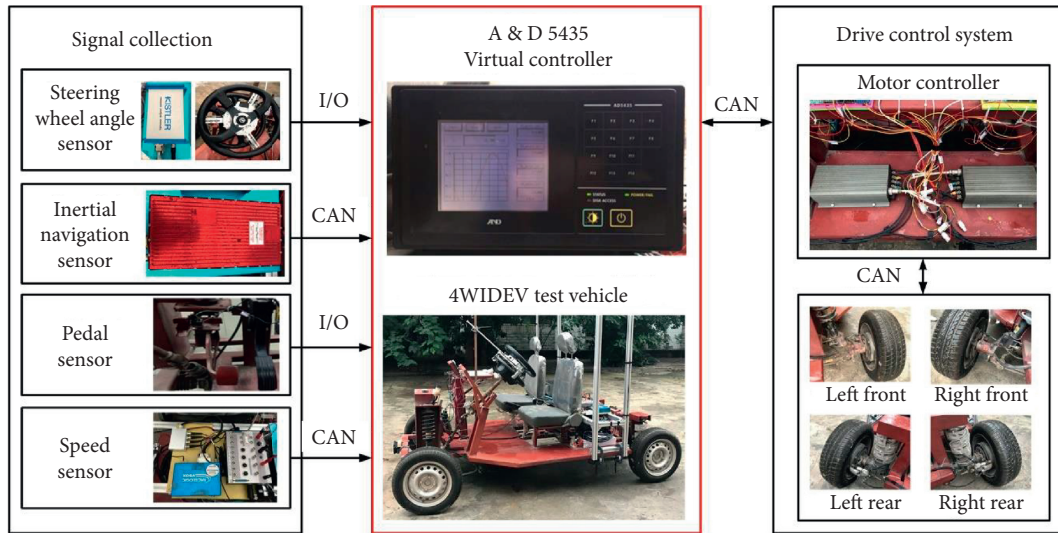


FIGURE 12: The road test scene.

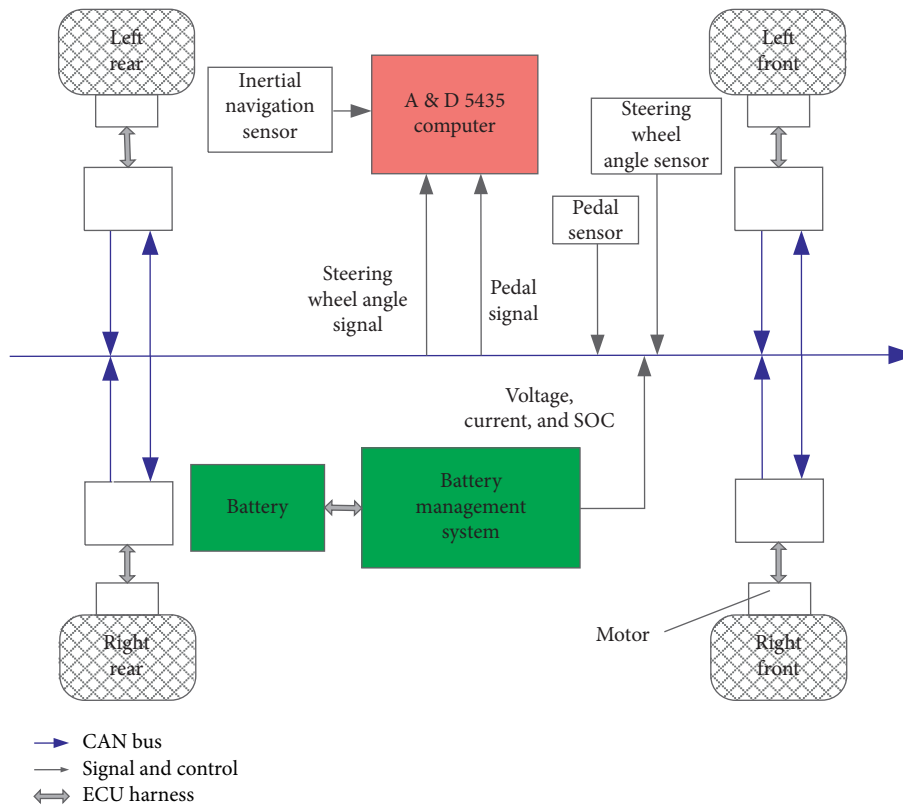


FIGURE 13: Configuration of the 4WIDEV test platform.

the A&D 5435 main include steering wheel angle, steering wheel angular speed, accelerator pedal opening, vehicle speed, acceleration, and vehicle attitude. As shown in Figure 12, the steering wheel angle and angular speed are collected by the Kistler CMSWB. The accelerator pedal opening is obtained by using the PASST B5 accelerator. These signals are input to the A&D 5435 by I/O port. The Racelogic VGPSBOX 3I is used to measure vehicle speed.

The Oxford RT 3100 inertial navigation measuring system is equipped to measure the vehicle attitude and acceleration. These signals are transmitted to the A&D 5435 through CAN bus. Because the DGPS, which can directly measure the side slip angle, and the tire force sensor have not been equipped on the test vehicle, with the consideration of the side slip angle and yaw rate being the key characteristic parameters for vehicle stability, the road test is utilized to verify the

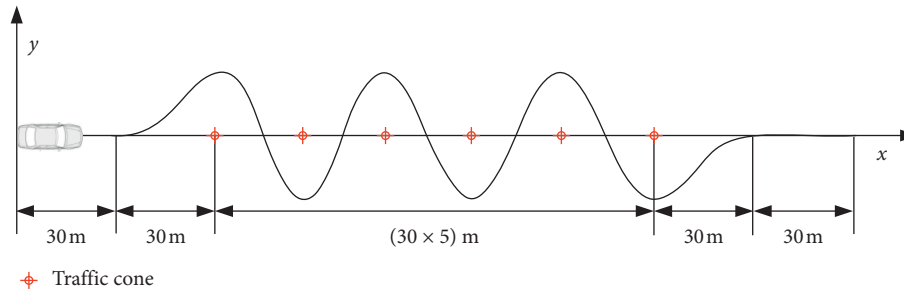


FIGURE 14: The trajectory of the serpentine maneuver.

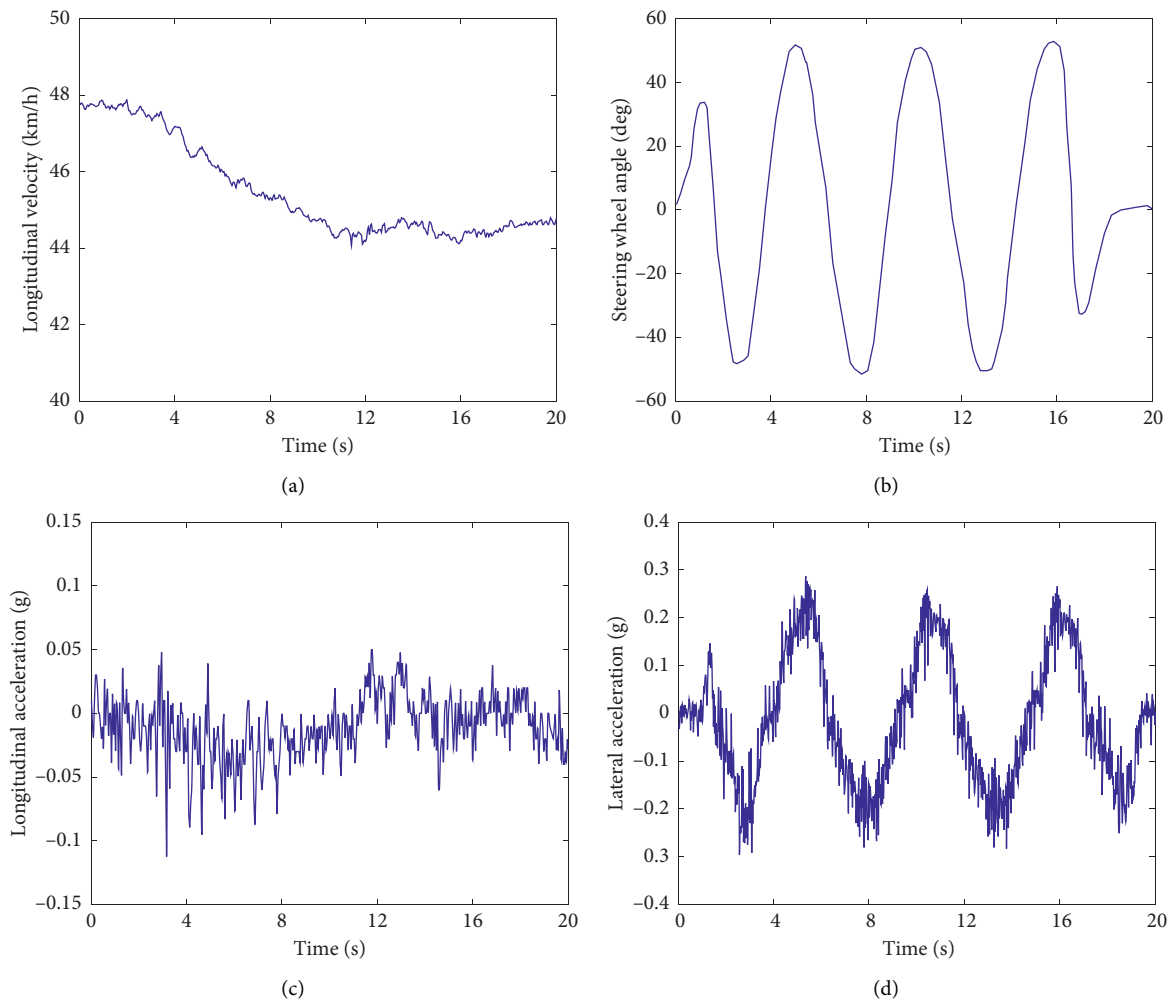


FIGURE 15: Vehicle states of road test: (a) longitudinal velocity; (b) steering wheel angle; (c) longitudinal acceleration; (d) lateral acceleration.

estimation performance of the yaw rate and side slip angle. Meanwhile, the side slip angle generated from CarSim will be taken as the reference measurement value for comparison.

The serpentine maneuver, which is a typical vehicle stability test condition, is selected to be carry out the vehicle experiment on the dry and asphalt road. The driving trajectory is shown in Figure 14, and a traffic cone is placed every 30 meters. The parameters of the road test vehicle are the same as those of the simulation vehicle. The driver will

maintain the longitudinal vehicle velocity in 45 ± 5 km/h, and the road coefficient is approximately 0.8.

Figure 15 shows the response curve of longitudinal vehicle velocity, steering wheel angle, and longitudinal and lateral acceleration in the road test. It can be seen in Figure 15(b) that there exist continuous fluctuations of steering wheel angle, and the maximum is about 50 deg. Figure 16(a) shows the comparison between the estimation value and the measurement of yaw rate. Figure 16(b) shows

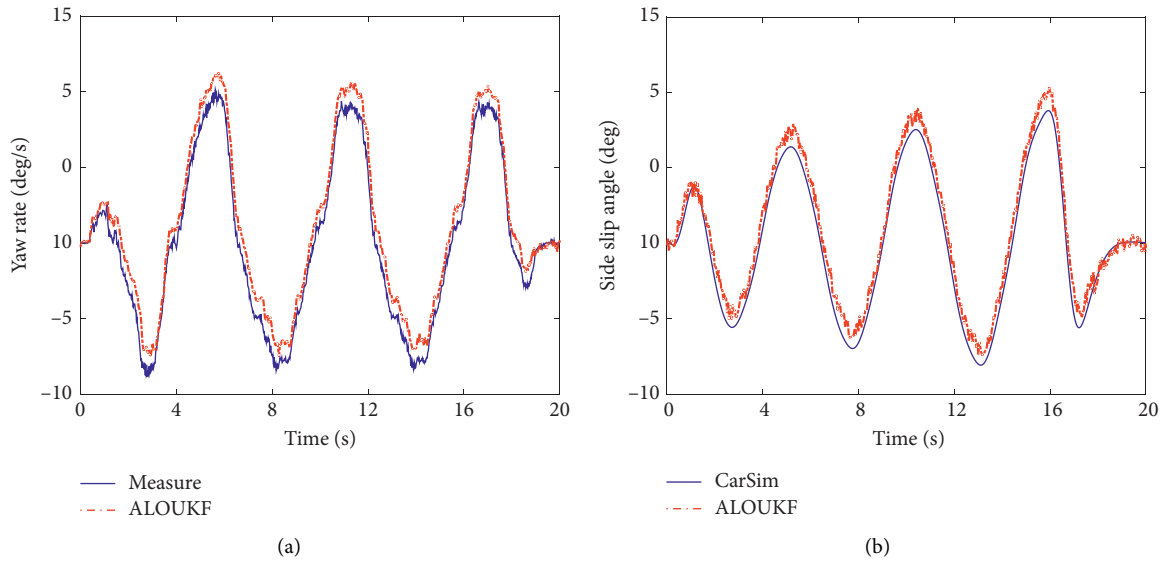


FIGURE 16: Estimation results of road test: (a) yaw rate; (b) side slip angle.

TABLE 8: Comparison of ME and RMSE for tire-road lateral force.

State	ME	RMSE
γ (deg/s)	2.8347	1.1405
β (deg)	0.1837	0.0956

the comparison between the reference value from CarSim with the estimation value of side slip angle. Table 8 shows the ME and RMSE of side slip angle and yaw rate.

As shown in Figure 16, similar to the simulation, the ALOUKF estimator performs well in the estimation of side slip angle and yaw rate in the road test. Notably, the estimation deviation becomes large when the vehicle turns, especially in the peak of the steering wheel angle; it can be seen in Table 8 that the ME of side slip angle and yaw rate is 0.1837 deg and 2.8347 deg/s, respectively. This is because of the inevitable model error when the vehicle state changes dramatically at the continuous cornering condition. But in general, the ALOUKF estimator can satisfy the requirement of estimation accuracy, as well as resist this dramatic change, as shown in Table 8, and the RMSE of side slip angle and yaw rate is 0.0956 deg and 1.1405 deg/s, respectively. This road test provides the effectiveness and feasibility of the proposed state estimation method. The results confirm that the ALOUKF estimator has good estimation accuracy even in the complicated and emergency condition; therefore, it can meet the requirements of vehicle stability control in the real application.

5. Conclusions

In this paper, we proposed a modified UKF methodology combining the ALO optimization algorithms for the vehicle state estimation in the application of 4WIDEV. The main findings can be concluded as follows:

- (1) To analyze the feasibility of the ALO algorithm for the identification of the system noise, both unimodal and multimodal optimization test functions were applied

and optimized by the GA, PSO, and ALO algorithms, respectively. The optimization result indicated that ALO has superior global optimization performance and better applicability for various problems.

- (2) The ALO algorithm was embedded into the UKF to adjust the statistical properties of measurement and process noise for the ALOUKF estimator design. The simulation of double lane change and sine wave steering maneuvers was carried out on the Matlab/Simulink-CarSim co-simulation platform. The serpentine maneuver road test was conducted on the RPP based on the A&D 5435 semiphysical simulation system and Matlab/Simulink code generation technology. The simulation and experiment results verify both the effectiveness and estimation accuracy improvement by using the proposed methodology compared with the conventional estimation method, of which the RMSE of side slip angle was decreased by 41.21% and 53.26% compared with the UKF and EKF, respectively, under the double lane change condition. Moreover, the ALOUKF estimator can resist vehicle nonlinearity even in complicated and emergency conditions.

In the future, more vehicle states and parameters will be considered to be estimated, such as the road adhesion coefficient. In addition, more attention will be focused on the road test validation of the tire lateral forces.

Data Availability

The data used to support the findings of this study are available from the corresponding author upon request.

Conflicts of Interest

The authors declare that there are no conflicts of interest regarding the publication of this paper.

Acknowledgments

The authors would like to express sincere gratitude to all those who supported them and also acknowledge the support of the Youth Innovation Team of Shaanxi Universities. This research was funded by the National Key Research and Development Program of China (grant no. 2019YFB1600800), the Key Research and Development Program of Shaanxi (grant nos. 2019ZDLGY15-01 and 2020ZDLGY16-01), the Youth Program of National Natural Science Foundation of China (52002034), and the Natural Science Basic Research Program of Shaanxi (grant no. 2020JQ-381).

References

- [1] P. Liu, Z. Y. Sun, and Z. P. Wang, "Entropy-based voltage fault diagnosis of battery systems for electric vehicles," *Energies*, vol. 11, no. 1, Article ID 136, 2018.
- [2] X. Zhao, X. M. Zhao, and Q. Yu, "Development of a representative urban driving cycle construction methodology for electric vehicles: a case study in Xi'an," *Transportation Research Part D-Transport and Environment*, vol. 81, Article ID 102279, 2020.
- [3] L. Geng, Y. Xiao, S. Li, H. Chen, and X. Chen, "Effects of injection timing and rail pressure on particulate size-number distribution of a common rail DI engine fueled with fischer-tropsch diesel synthesized from coal," *Journal of the Energy Institute*, 2020.
- [4] X. Zhao, Y. Ye, J. Ma, P. Shi, and H. Chen, "Construction of electric vehicle driving cycle for studying electric vehicle energy consumption and equivalent emissions," *Environmental Science and Pollution Research*, vol. 27, no. 30, Article ID 37395, 2020.
- [5] B. Zhang, H. Du, J. Lam, N. Zhang, and W. Li, "A novel observer design for simultaneous estimation of vehicle steering angle and sideslip angle," *IEEE Transactions on Industrial Electronics*, vol. 63, no. 7, pp. 4357–4366, 2016.
- [6] S. B. Phadke, P. D. Shendge, and V. S. Wanaskar, "Control of antilock braking systems using disturbance observer with a novel nonlinear sliding surface," *IEEE Transactions on Industrial Electronics*, vol. 67, no. 8, pp. 6815–6823, 2020.
- [7] H. Zhang, J. Liang, H. Jiang, Y. Cai, and X. Xu, "Stability research of distributed drive electric vehicle by adaptive direct yaw moment control," *IEEE Access*, vol. 7, pp. 106225–106237, 2019.
- [8] W. Zhao, M. Fan, C. Wang, Z. Jin, and Y. Li, " H^∞ /extension stability control of automotive active front steering system," *Mechanical Systems and Signal Processing*, vol. 115, pp. 621–636, 2019.
- [9] M. S. Chae, Y. J. Hyun, and K. S. Yi, "Dynamic handling characteristics control of an in-wheel-motor driven electric vehicle based on multiple sliding mode control approach," *IEEE Access*, vol. 7, pp. 132448–132458, 2019.
- [10] E. Regolin, A. Alatorre, M. Zambelli, A. Victorino, A. Charara, and A. Ferrara, "A sliding-mode virtual sensor for wheel forces estimation with accuracy enhancement via EKF," *IEEE Transactions on Vehicular Technology*, vol. 68, no. 4, pp. 3457–3471, 2019.
- [11] G. Reina and A. Messina, "Vehicle dynamics estimation via augmented extended Kalman filtering," *Measurement*, vol. 133, pp. 383–395, 2019.
- [12] X. L. Shao, H. N. Si, and W. D. Zhang, "Fuzzy wavelet neural control with improved prescribed performance for MEMS gyroscope subject to input quantization," *Fuzzy Sets and Systems*, 2020.
- [13] B. Lenzo, F. Bucchi, A. Sorniotti, and F. Frendo, "On the handling performance of a vehicle with different front-to-rear wheel torque distributions," *Vehicle System Dynamics*, vol. 57, no. 11, pp. 1685–1704, 2018.
- [14] J. Y. Lv, H. W. He, and W. Liu, "Vehicle velocity estimation fusion with kinematic integral and empirical correction on multi-timescales," *Energies*, vol. 12, no. 1242, Article ID 1242, 2019.
- [15] A. Rezaeian, A. Khajepour, W. Melek, S.-K. Chen, and N. Moshchuk, "Simultaneous vehicle real-time longitudinal and lateral velocity estimation," *IEEE Transactions on Vehicular Technology*, vol. 66, no. 3, pp. 1950–1962, 2017.
- [16] D. M. Bevly, J. Ryu, and J. C. Gerdes, "Integrating INS sensors with GPS measurements for continuous estimation of vehicle sideslip, roll, and tire cornering stiffness," *IEEE Transactions on Intelligent Transportation Systems*, vol. 7, no. 4, pp. 483–493, 2006.
- [17] J. Ryu and J. C. Gerdes, "Integrating inertial sensors with global positioning system (GPS) for vehicle dynamics control," *Journal of Dynamic Systems, Measurement, and Control*, vol. 126, no. 2, pp. 243–254, 2004.
- [18] J. Ryu and J. C. Gerdes, "Estimation of vehicle roll and road bank angle," in *Proceedings of the 2004 American Control Conference*, pp. 2110–2115, Boston, MA, USA, June 2004.
- [19] D. Selmaj, M. Corno, and G. Panzani, "Robust vehicle sideslip estimation based on kinematic consideration," in *Proceedings of the 20th World Congress of the International-Federation-Of-Automatic-Control (IFAC)*, pp. 14855–14860, Toulouse, France, July 2017.
- [20] D. Selmaj, M. Corno, and G. Panzani, "Vehicle sideslip estimation: a kinematic based approach," *Control Engineering Practice*, vol. 67, pp. 1–12, 2017.
- [21] R. V. Marco, J. Kalkkuhl, and J. Raisch, "Multi-modal sensor fusion for highly accurate vehicle motion state estimation," *Control Engineering Practice*, vol. 100, Article ID 104409, 2020.
- [22] F. Auger, M. Hilairet, J. M. Guerrero, E. Monmasson, T. Orłowska-Kowalska, and S. Katsura, "Industrial applications of the Kalman filter: a review," *IEEE Transactions on Industrial Electronics*, vol. 60, no. 12, pp. 5458–5471, 2013.
- [23] G. Baffet, A. Charara, and D. Lechner, "Estimation of vehicle sideslip, tire force and wheel cornering stiffness," *Control Engineering Practice*, vol. 17, no. 11, pp. 1255–1264, 2009.
- [24] G. Baffet, A. Charara, D. Lechner, and D. Thomas, "Experimental evaluation of observers for tire-road forces, sideslip angle and wheel cornering stiffness," *Vehicle System Dynamics*, vol. 46, no. 6, pp. 501–520, 2008.
- [25] X. Li, C.-Y. Chan, and Y. Wang, "A Reliable fusion methodology for simultaneous estimation of vehicle sideslip and yaw angles," *IEEE Transactions on Vehicular Technology*, vol. 65, no. 6, pp. 4440–4458, 2016.
- [26] S. J. Julier and J. K. Uhlmann, "Unscented filtering and nonlinear estimation," *Proceedings of the IEEE*, vol. 92, no. 3, pp. 401–422, 2004.
- [27] S. Antonov, A. Fehn, and A. Kugi, "Unscented Kalman filter for vehicle state estimation," *Vehicle System Dynamics*, vol. 49, no. 9, pp. 1497–1520, 2011.
- [28] X. Jin and G. Yin, "Estimation of lateral tire-road forces and sideslip angle for electric vehicles using interacting multiple model filter approach," *Journal of the Franklin Institute*, vol. 352, no. 2, pp. 686–707, 2015.
- [29] H. Heidfeld, M. Schünemann, and R. Kasper, "UKF-based state and tire slip estimation for a 4WD electric vehicle," *Vehicle System Dynamics*, vol. 58, no. 10, pp. 1479–1496, 2019.

- [30] G. Reina, A. Leanza, and A. Messina, "Terrain estimation via vehicle vibration measurement and cubature Kalman filtering," *Journal of Vibration and Control*, vol. 26, no. 11-12, pp. 885–898, 2020.
- [31] H. E. Soken and C. Hajiyev, "Adaptive fading UKF with Q-adaptation: application to picosatellite attitude estimation," *Journal of Aerospace Engineering*, vol. 26, no. 3, pp. 628–636, 2013.
- [32] T. Chen, Y. Cai, L. Chen, X. Xu, H. Jiang, and X. Sun, "Design of vehicle running states-fused estimation strategy using Kalman filters and tire force compensation method," *IEEE Access*, vol. 7, pp. 87273–87287, 2019.
- [33] Z. Wang, Y. Qin, L. Gu, and M. Dong, "Vehicle system state estimation based on adaptive unscented Kalman filtering combining with road classification," *IEEE Access*, vol. 5, pp. 27786–27799, 2017.
- [34] E. S. Ali, S. M. Abd Elazim, and A. Y. Abdelaziz, "Ant lion optimization algorithm for renewable distributed generations," *Energy*, vol. 116, pp. 445–458, 2016.
- [35] T. Tian, C. Y. Liu, and Q. Guo, "An improved ant lion optimization algorithm and its application in hydraulic turbine governing system parameter identification," *Energies*, vol. 11, no. 1, Article ID 95, 2018.
- [36] E. S. Ali, S. M. Abd Elazim, and A. Y. Abdelaziz, "Ant lion optimization algorithm for optimal location and sizing of renewable distributed generations," *Renewable Energy*, vol. 101, pp. 1311–1324, 2017.
- [37] S. Mirjalili, P. Jangir, and S. Saremi, "Multi-objective ant lion optimizer: a multi-objective optimization algorithm for solving engineering problems," *Applied Intelligence*, vol. 46, no. 1, pp. 79–95, 2016.
- [38] Q. W. Zhong, Q. Y. Dan, and H. Y. Xiao, "Parameter identification of photovoltaic cell model based on improved ant lion optimizer," *Energy Conversion and Management*, vol. 151, pp. 107–115, 2017.
- [39] S. Mirjalili, "The ant lion optimizer," *Advances in Engineering Software*, vol. 83, pp. 80–98, 2015.
- [40] Z. Qi, S. Taheri, B. Wang, and H. Yu, "Estimation of the tyre-road maximum friction coefficient and slip slope based on a novel tyre model," *Vehicle System Dynamics*, vol. 53, no. 4, pp. 506–525, 2015.
- [41] S.-L. Koo and H.-S. Tan, "Tire dynamic deflection and its impact on vehicle longitudinal dynamics and control," *IEEE/ASME Transactions on Mechatronics*, vol. 12, no. 6, pp. 623–631, 2007.
- [42] C. Wei and O. A. Olatunbosun, "The effects of tyre material and structure properties on relaxation length using finite element method," *Materials & Design*, vol. 102, pp. 14–20, 2016.
- [43] R. R. Rani and D. Ramyachitra, "Antlion optimization algorithm for pairwise structural alignment with bi-objective functions," *Neural Computing and Applications*, vol. 32, no. 11, pp. 7079–7096, 2020.
- [44] J. Wang, P. Du, H. Lu, W. Yang, and T. Niu, "An improved grey model optimized by multi-objective ant lion optimization algorithm for annual electricity consumption forecasting," *Applied Soft Computing*, vol. 72, no. 2, pp. 321–337, 2018.
- [45] J. Bossek, "Smoof: single- and multi-objective optimization test functions," *The R Journal*, vol. 9, no. 1, pp. 103–113, 2017.
- [46] S. Mishra, "Some new test functions for global optimization and performance of repulsive particle swarm method," University Library of Munich, Munich, Germany, MPRA Paper, 2006.